Nanocoatings

Technology of Fabrication of Nanostructure (Nanocomposite) Coatings with High Physical and Mechanical Properties Using C-PVD

A.D. Pogrebnjak, O.V. Bondar, N.A. Azarenkov, V.M. Beresnev, O.V. Sobol, and N.K. Erdybaeva

CONTENTS

INTRODUCTION

Hard nanostructure coatings are rather effective in increasing of productivity, improving of wear resistance and durability of metals and alloys. Due to its perfect unique mechanical properties and thermal stability, the protective layer noticeably supports and improves the functional state of instruments and devices under extreme conditions of exploitation. Such protective coatings allow having high hardness, low values of friction coefficient, good adhesion to the substrate, and high level of oxidation and wear resistance of operating parts of different instruments and devices. The most popular and widely used methods of protective coating fabrication are vacuum-arc deposition, ion metallization, and magnetron sputtering [1–4].

Nitrides of transitive metals are widely used in industry as protective coatings from the end of the twentieth century. Titanium nitride (TiN) is the most popular material among the other binary systems of nitrides due to its significantly high mechanical properties and corrosion resistance. Titanium–aluminum nitride ($Ti_{1-x}Al_xN$) became very popular in the last decade because it can be used to improve hardness and durability of blades of cutting instruments for high-speed processing. Moreover, the presence of aluminum increases oxidation resistance of covered materials in the temperature range 500°C ÷ 800°C. Also it leads to the formation of a thick interlayer of aluminum oxide. Adding chromium or zirconium to TiN (separately or together) forms triple Ti–Cr–N and Ti–Zr–N systems and also improves physical and mechanical properties. Thus, conversion from binary coatings to more complex systems (triple, quadruple etc.) by doping transitive metal nitrides of corresponding elements is a very effective method of improving the coating's physical, mechanical, and tribotechnical properties and their resistance to high-temperature oxidation.

Developing multilayer periodical systems seems to be the next step in the universalization of nitride material properties. It is also very important to fabricate four- and five-element coatings, with three or four transition metals and nitrogen as a filling element with powerful covalent connections. During the last 7–9 years, high-entropy alloys were conceived. In some papers such materials are called multicomponent. A stable structure and composition and high exploitation characteristics of high-entropy systems lead to the fabrication of coatings, improving surface characteristics, and to using them as protective films, which are able to avoid harmful admixtures penetrating into the near-surface layer. Due to the effect of intensive mixing, entropy contribution increases in high-entropy alloys, and it is a reason to form a solid solution with a simple structure.

According to the aforementioned, studying of Ti–Si–N, Ti–Hf–N, Ti–Hf–Si–N, Ti–Zr–N, Ti–Zr–Si–N, and high-entropy

(Ti–Hf–Zr–V–Nb)N coatings is an actual task of modern materials science. In this chapter we present the results of deposition and investigation of such coatings.

DEPOSITION REGIMES AND METHODS OF COATING ANALYSIS

Deposition Conditions and Regimes

We consider several types of coatings: Ti–Si–N, Ti–Hf–Si–N, Zr–Ti–Si–N, and Ti–Zr–Hf–V–Nb–N. For the coating deposition process, we used a cathodic arc vapor deposition device AQ1 "Bulat-3T" with HF generator [7,9]. Potential bias was applied to the substrate from the HF generator of pulsed damped oscillations, and its frequency was less than 1 MHz. The duration of each pulse was 60 μs; the repetition rate was about 10 kHz. The amount of negative self-bias potential of the substrate caused by the HF diode effect was 2–3 kV. Using three steel samples (2 mm thickness, 20 mm diameter, polished surface), we deposited coatings on the device with cathodic vacuum-arc vaporizer in high-frequency discharge (two cathodes, made of Ti and Si). Atomic nitrogen was injected into the chamber. The thickness of the obtained coating was near 2.2 μm.

For TiN coating fabrication, we used Ti of grade BT-1-00. The thickness of all coatings was 2.2 μm. The deposition parameters are presented in the Table 1.

Samples of Ti–Hf–Si–N composition were deposited on substrates made of steel (St. 3–0.3 wt% C; the rest is Fe) with polished surface of 20 mm diameter and 3 mm thick in a vacuum chamber with a vacuum in HF discharge, where a cathode made of sintered Ti_{35}–Hf_{18}–Si_{13} was used. To obtain nitrides the acceleration chamber was filled with atomic nitrogen at different pressures (see Table 2).

Deposition of Ti–Zr–Hf–V–Nb–N coatings was performed by the cathode vacuum-arc deposition method on the Bulat-6 device [8] under constant negative potential U_s = (−40–200) V, which was applied to a substrate. The arc current did not exceed 85 A, and the pressure of residual gas was 0.0066 Pa. The deposition parameters, which were employed for all Ti–Zr–Hf–V–Nb–N samples, are presented in Table 3.

Thermal annealing of coatings was performed in the furnace VacuTherm-Ceram VT 1200 at temperature 873 K for 30 min. Residual pressure P was 100 Pa.

Methods of Coating Analysis

Phase composition and structure researching were provided on the x-ray diffractometer DRON-3M and Rigaku RINT-2500, MDG, Japan, in Cukα irradiation using a graphite monochromator in secondary beam. Diffraction spectrums were obtained in pointwise regime with a scanning step 2θ = 0.05…0.10. We also employed the diffraction of x-rays using a grazing incidence beam, in Cr emission, at angle 3°. For stress analysis, we used x-ray tensometry (α-$\sin^2\psi$ method) and its modifications, which are valid for coatings with strong axial-type texture [15,16].

The elementary composition of the Ti–Si–N coatings was studied using Rutherford backscattering (RBS) of $^4He^+$ AQ2 ions with 1.7 MeV energy, detector resolution E = 13 keV, and scattering angle ≈ 170°. Secondary ion mass spectrometry (SIMS), SAJW-05 spectrometer with quadrupole mass analyzer QMA-410 Balzers, and glow discharge mass spectrometry (GDMS), SMWJ-01 spectrometer with quadrupole mass analyzer SRS-300 (Warsaw, Poland), were also applied [27,28]. To obtain complete information about the elemental composition of Ti–Hf–Si–N coatings, the RBS scheme of He^+ AQ3

TABLE 1
Physical and Technical Parameters of Deposition of Ti–Si–N Coatings

Deposited Material	Coating	I, A	P_N, Pa	U_{hf}, V	U_b, B	Remarks
Ti	TiN	90	0.3	200	200	High-frequency pulse
Ti+Si	Ti–Si–N	100	0.3	200	—	technology
Ti+Si	Ti–Si–N	100	0.7	200	—	

TABLE 2
Deposition Parameters for Different Sample Series of Ti–Hf–Si–N Coatings

Sample Series	No	Nitrogen Pressure P in Chamber, Pa	Potential on Substrate, V
1	23 (separated)	0.7	−200
3	28 (direct)	0.6–0.7	−200
	35 (direct)	0.6–0.7	−100
1	37 (separated)	0.6	−100
	31 (separated)	0.3	−200
2	10 (separated)	0.5	−180
	11 (separated)	0.7	−150

TABLE 3
Deposition Parameters for Different Sample Series of Ti–Zr–Hf–V–Nb–N Coatings

				Concentration, %					
No	Material	U_{bias}, V	P, Pa	N	Ti	V	Zr	Nb	Hf
505	Ti–Zr–Hf–V–Nb–N	110	0.5×10^{-1}	49.15	16.63	5.91	8.17	8.88	11.26
506	Ti–Zr–Hf–VNb–N	100	0.2×10^{-1}	49.05	22.92	5.04	6.84	7.47	8.68
507	Ti–Zr–Hf–V–Nb–N	50	5×10^{-2}	51.13	25.31	4.72	5.70	6.31	6.84
509	Ti–Zr–Hf–V–Nb–N	100	3×10^{-1}	44.7	25.31	4.57	7.60	7.99	9.83
510	Ti–Zr–Hf–V–Nb–N	50	2×10^{-1}	49.11	19.67	5.65	7.68	8.24	9.64
512	Ti–Zr–Hf–V–Nb–N	200	8×10^{-2}	46.65	17.03	2.79	12.01	12.54	8.98
513	Ti–Zr–Hf–V–Nb	40	8×10^{-2}	—	34.66	8.88	19.53	23.16	13.76
514	Ti–Zr–Hf–V–Nb–N	200	2×10^{-1}	47.69	16.41	1.93	13.34	13.90	6.72
515	Ti–Zr–Hf–V–Nb–N	200	3×10^{-2}	36.05	20.13	2.28	17.12	17.50	6.93
523	Ti–Zr–Hf–V–Nb–N	200	2×10^{-1}	43.44	17.80	1.45	16.39	16.99	3.92

ions with an energy of 1.3 MeV (scattering angle θ = 170°; for normal incidence of probing ions on the samples, the energy resolution of the detector is 16 keV) was used. The dose of helium ions was 5 μC. For interpretation of RBS spectra, the standard (international) program [13] of element profiles in depth measurement was used. To provide the elemental analysis, a different accelerator (RBS) with He^+ions with energies of 1.7 MeV was used. The program used to interpret the spectra was SIMNRA [21] (Dresden, Germany).

We also used scanning electron microscopy (SEM) with energy dispersion analysis (JEOL 7000F microscope, Japan) in contrast of electrons and in direct and backscattering electron reflection. Transmission electron microscope JEOL 2010 F was also used for structure analysis of coatings. For surface morphology investigations, we used atomic force microscopy (AFM), electron-ion scanning microscope Quanta 200 3D with Roentgen-fluorescent microanalyzer EDAX with appropriate software, and automatic contact precision profilometer SURTRONIC 25 to obtain a 3D image of the surface topography.

Nanohardness and elastic modulus measurements were done using trihedral Berkovich indenter (Nano Indenter G200, MES Systems, Nano Instruments Innovation Center, Oak Ridge, USA) with a three-sided Berkovich diamond pyramid with a radius of about 20 nm blunting the apex. The accuracy of the depth measurement was ±0.4 nm. To reduce the influence of the substrate on the measured hardness of samples, the indentation was carried out to a depth of 200 nm. In this case, the prints were applied at 15 μm apart. At least five measurements using continuous stiffness monitoring module CMA (continuous stiffness measurement) were made on each sample. The depth of the indentation was much less than 1/10 of the coating film's thickness [8]. Analysis of the load curve was made by the well-known method of Oliver and Pharr.

Friction test by the "finger-surface" method was held at the TAU-1M tribometer under dry friction conditions. The friction coefficient and wear resistance of films were determined by the reciprocating sliding, performed at room temperature (22°C ± 1°C) and relative humidity of 80% ± 5%. The velocity of the plate and the sample was 4 mm/s, the rounded indenter

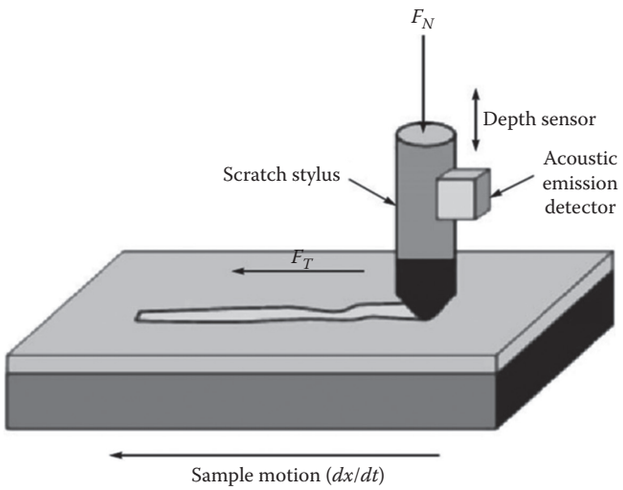

FIGURE 1 Experimental device for the determination of the adhesive/cohesive strength. Designations: F_N is the normal load and F_T is the friction force.

radius of the curvature of 0.5 mm was made of hard metal VK8 (hardness of 87.5 HRC), and the load on the indenter was 1 N. To determine the adhesive/cohesive strength and scratch resistance and also to study the fraction mechanism, the scratch tester REVETEST (CSM Instruments) [22] was used (Figure 1). The scratches were applied to the coating surface at continuously increasing load by diamond spherical indenter "Rockwell C" with a radius of curvature of 200 μm. Simultaneously the power of acoustic emission, the friction coefficient and the penetration depth of the indenter, and the value of the normal load (F_N) were recorded. Three scratches were applied to each sample.

Tests were carried out under the following conditions: the load on the indenter was increased from 0.9 to 70 N, the speed of the indenter movement 1 mm/min, the scratch length −10 mm, the loading rate −6.91 N/min, the frequency of a digital signal 60 Hz, and acoustic emission 9 Db. The tests determined the minimum (critical) load L_{C1}, which corresponds to the beginning of the indenter penetration into

the coating; L_{C2}, top when the first cracks appear; L_{C3}, the peel of some parts of coating; and L_{C4}, plastic abrasion of the coating to the substrate. Registration, during a test (a relatively large number of different physical parameters), improves the reliability and accuracy of the method of the critical load determination. The deformation of the coating by the diamond indenter was investigated further using the integrated optical microscope and electron-ion scanning microscope Quanta 200 3D, equipped with an integrated system of Pegasus 2000 for microanalysis. Also we used for tribological tests an automated friction machine "Tribometer" (CSM Instruments) in air by the "ball-disk" scheme at 293 K. The ball with a diameter of 6 mm was made of sintered certificated material—Al_2O_3. The coatings were deposited on steel (45 HRC = 55) disks with a diameter of 50 mm and a thickness of 5 mm. The load was 3.0 N, with sliding velocity 10 cm/s.

For analysis of vacancy-type defects in the coating, we used slow positron beam—so-called positron annihilation spectroscopy (PAS) (Halle, Germany). We measured the *S*-parameter of the Doppler broadening annihilation peak (DBAP) by changing the energy of the fallen positron beam from 1 to 30 KeV, and that allowed us to change the analysis depth [2,14] from a few nm to 2.1 μm [15,24,25]. The bonding states were determined using photoelectron spectroscopy (XPS, Kratos AXIS Ultra) with a monochromatic AlKα (1486.71 eV, x-ray radiation 15 kV/10 mA).

X-ray diffraction analysis of nanostructured coatings was carried out on two devices: DRON-4 (Russian Federation) and X'Pert PANalytical (Holland). The step size is 0.05°, displacement speed is 0.05°, $U = 40$ kV, $I = 40$ mA, and the cathode is copper. Cross sections of the *coating–substrate* system were prepared by an ion beam. On these cross sections, the morphology, structure, and elemental composition of coatings were analyzed.

CHANGING OF THE DEFECT'S STRUCTURE AND PROPERTIES OF SUPERHARD NANOSTRUCTURED TI–SI–N COATINGS, FABRICATED USING CPVD, BEFORE AND AFTER ANNEALING

Fragments of diffraction spectrums for Ti–Si–N samples (as deposited and after annealing under the temperature 600°C for 30 min) are presented on Figure 2. We calculated lattice parameter $a_0 = 0.42462$ Å and found strong texture (111) (Ti, Si) N and (222) (Ti, Si) N (see curves 1 and 2). In addition, we detected small peaks from TiO_2 (JCPDS-19-370). The volume fraction of oxides after thermal annealing in the chamber is low and it is not higher than 5%.

Stress analysis showed that there is high compression deformation in (Ti, Si) N hard solution (equal to −2.6%) and it is reduced to the value of −2.3% after annealing. Coherent-scattering region evaluation (using Sherrer methodic) showed that the size of the nanograins increased from 12.5 to 13 nm, and when the initial size of nanograins is 25 nm, it increased to

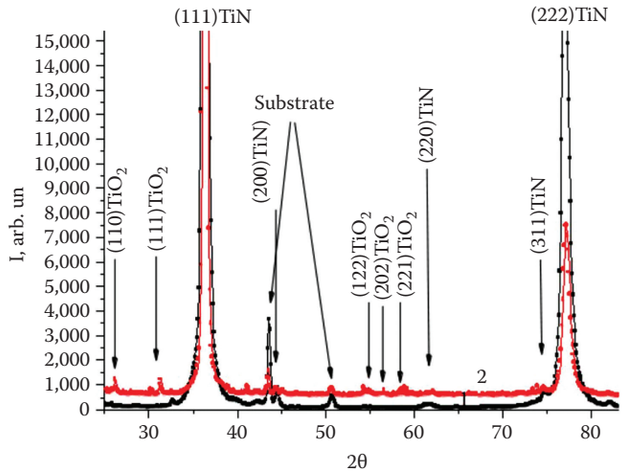

FIGURE 2 Ti–Si–N coating's x-ray diffraction patterns: (a) as deposited and (b) after annealing under the temperature of 600°C for 30 min; vacuum $P = 50$ mbar.

28–30 nm. In other words, due to annealing under the temperature of 600°C for 30 min, insignificant changing of grain size is observed, and rest of the energy was used on finishing of the spinodal segregation process, forming an α-Si_3N_4 monolayer. We can make an interim conclusion that when compression deformation and the order of structuring are high, annealing under the temperature of 600°C for 30 min does not lead to catastrophic changes in the phase composition, structure, and mode of deformation. A layer, made of (Ti, Si)N solid solution, is formed, and the silicon–nitrogen phase is also formed around nanograins. In according to it, the Si concentration is reduced in solid solution; some amount of Ti atoms creates TiO_2 film on the coating's surface.

The Ti–Si–N coating structure is characterized by a high level of microdeformations of lattice (more than 1%) [13]. A high value of microdeformations of lattice probably indicates inhomogeneity of the chemical structure in every phase of the coating.

Coatings have a strong texture [10]. Condensation of compressive stresses leads to (111) texture forming in (Ti, Si) N solid solution films. Using approximation methods, we defined the average crystallite sizes of the (Ti, Si)N solid solution, which varies from 12.5 to 25 nm. The obtained coatings have the following hardness: TiN ($H = 28$ GPa, $E = 312$ GPa) and Ti–Si–N ($H = 38$–39 GPa, $E = 356$ GPa).

In Table 4 we summarized the results of tribological investigations. It is clearly seen from these results that the wear coefficient for TiN coating increases with temperature increasing, but for Ti–Si–N coating, the wear coefficient decreases to 0.69 ($T = 500$°C), which is approximately 25% less than under room temperature.

Elementary analysis results are presented in Figure 3, which was obtained using the RBS method and energy-dispersive spectroscopy (EDS). As it is clearly seen from Figure 3a, the Si concentration is less than 5 at.%, N concentration ≈ (35–40) at.%, rest one is Ti, and for Figure 3b, N concentration ≈ 50 at.%, Ti ≈ 44 at.%, Si ≈ 5.5 at.%.

TABLE 4
Tribological Properties of Nanocomposite Coatings

Coating	Temperature,°C	Wear Factor, Coating, mm³/nm	Wear Factor, Counterbody mm³/nm	Friction Coefficient
Ti–Si–N	30	7.69×10^{-5}	3.28×10^{-5}	0.88
	300	2.63×10^{-5}	3.49×10^{-5}	0.82
	500	1.95×10^{-5}	2.75×10^{-5}	0.69
TiN	30	6.75×10^{-5}	3.30×10^{-5}	0.81
	300	3.62×10^{-5}	3.51×10^{-5}	0.87
	500	5.16×10^{-5}	3.83×10^{-5}	0.91

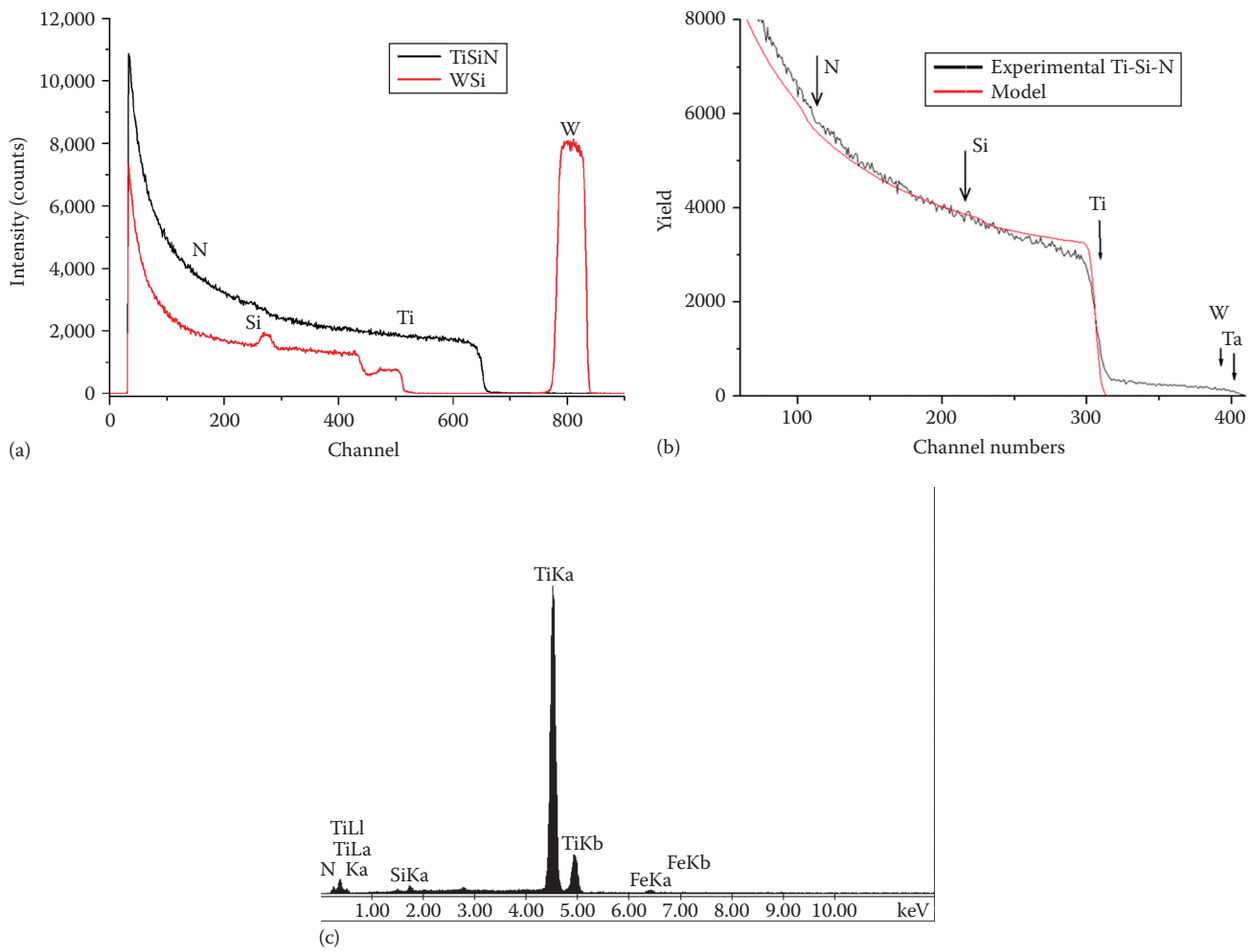

FIGURE 3 Energy spectrums for samples with Ti–Si–N coatings: (a) bias potential –50 V, P_N = 0.5 Pa (RBS), (the second curve corresponds to the etalon SiW curve [for comparison]); (b) bias potential –100 V, P_N = 0.7 Pa (RBS); and (c) bias potential –50 V, P_N = 0.5 Pa (EDX).

The coating's thickness equals to 2.18 ± 0.01 μm according to RBS data. RBS data are confirmed by EDX results (see Figure 3c). The concentration of Si in the coating is 2.62 at.%, Ti ≈ 40.69 at.%, N ≈ 55.92 at.%. For another series of samples (with Si concentration ≥5.8 at.%), we provided investigations of the Si–N*x* connection using XPS analysis. It showed high peak on 101.9 eV, and it points directly on the formation of the Si–N*x* connection in this sample. But we also had a small peak, which points on the formation of a very few amounts of Si–O on 103.9 eV (after annealing in air under the temperature of 600°C for 30 min). Additional μ-PIXE investigations showed SiN formation on TiN nanograin borders.

Images of the coating's surface before and after annealing, under the temperature 600°C (for 30 min), are presented in Figure 4. We can observe flat "drops" of melted phase, regardless of HF stimulation. We should note that part of the plasma jet consists of drop fractions, and we did not make analysis of such fractions. To obtain a real thickness of Ti–Si–N

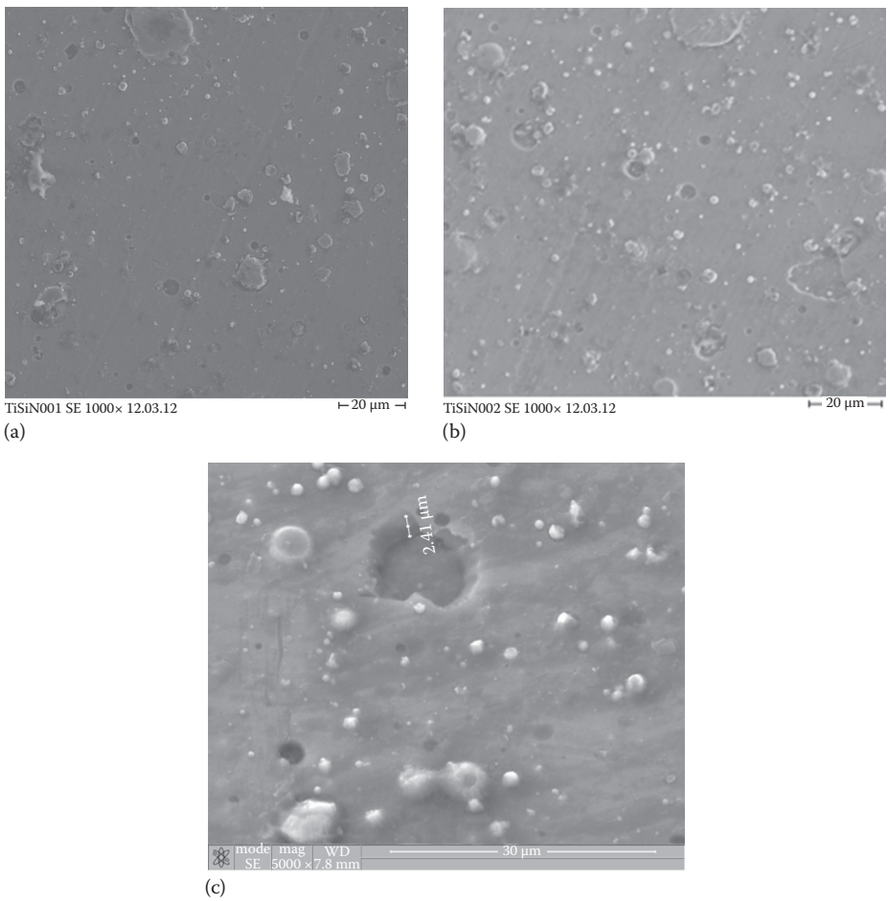

FIGURE 4 Surface topography of the Ti–Si–N coating: (a) as-deposited state, (b) after annealing under the temperature of 600°C, and (c) SEM analysis of circle cross section, which was obtained using ion beam cutting.

nanostructure coating and to norm the depth of slow positron beam analysis, we cut a circle hole, through the coating thickness. As it is seen from Figure 4c, coating thickness equals to 2.39–2.41 µm. Calculation of positron penetration depth shows that E_{max} = 20 keV, which corresponds to 2.11 µm of thickness. Even if we will take into account diffusion of thermalized positrons (its length is $L \approx 100$ nm), we will see that the positron beam cannot reach the interface between the coating and substrate. That is why profiles of mean positron's penetration depths give us information about vacancy-type defects on the whole thickness of the Ti–Si–N coating, but the interface border is not really achieved by them.

Positron annihilation method is the most effective, responsive, and reliable method of analysis of free volumes in nanocrystalline materials (it has possible interval of the defect's analysis in the range of $10^{-6} \pm 10^{-3}$ defects per atom) [2,14]. Part of positrons can be captured on the interface of two neighboring nanograins or on the boundary junction of three neighboring nanocrystals. It gives us a good opportunity to solve one of the most complicated and interesting problems of nanomaterials—to understand the structure (including electron structure) of the interfaces between nanograins, because the length (volume) of such interfaces influences the properties of nanocomposite coatings a lot [5–13].

Figure 5 shows the dependence of the *S*-parameter on energy; in other words, we can see profiles of defects in the Ti–Si–N coating before (black curve) and after (red curve) thermal annealing under the temperature of 600°C (30 min). Significant changes in electron and defect structure of the

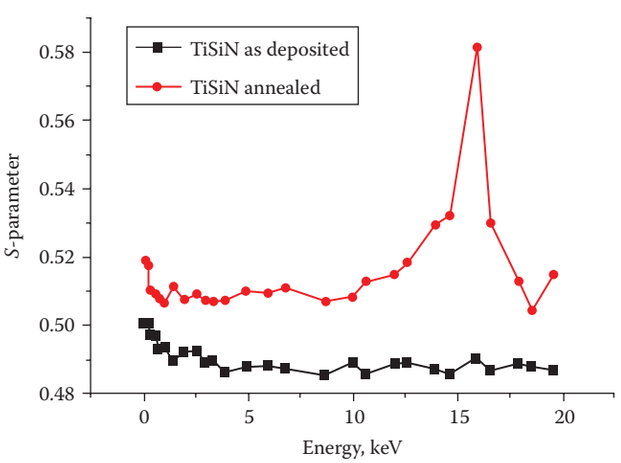

FIGURE 5 Dependence of the *S*-parameter on the energy of the positron microbeam (black curve, as-deposited coating; red curve, annealed coating). AQ6

coating are clearly seen from this figure. We should note that the defect's concentration increases on the whole thickness of the coating, and all positrons locate and annihilate on defects, which are situated on the boundaries of nanograins. The depth of diffusion of thermolized positrons is ≈100 nm, and the size of nanograins is 12.5–13 nm, so we can say that almost all positrons are captured on the interface's defects. Approaching the interface between the coating and substrate, the *S*-parameter significantly increases, that is, defects also migrate to the interface between the coating and substrate due to thermal diffusion. The thickness of this transition layer of defects is no more than 250 nm. Calculation of vacancy defect concentration was done using the positron capture model with two types of vacancy defects [12], and it showed that defect concentration increases after annealing from 5×10^{16} to 7.5×10^{17} cm^{-3} and thermally activated vacancy concentration also increases from 1×10^{16} to 5×10^{18} cm^{-3} (see red curve).

Loading and unloading curves are presented in Figure 6. The nanoindenter penetrates on the surface layer of the Ti–Si–N coating (three different loadings). As it is seen from calculations, based on the Oliver–Pharr method, an average hardness for such deposition regimes is 38.7 GPa and the elasticity modulus is 370 ± 12 GPa. Annealing under the temperature of 600°C in vacuum leads to increase of elasticity modulus to values of 430–448 GPa, which is connected with finishing of process of spinodal segregation on the boundaries of nanograins, that is, with forming of thin SiN (Si_3N_4) interlayer (amorphous and quasi amorphous phases). Moreover, thermal annealing under the temperature of 600°C in vacuum also changes the Ti–Si–N coating's surface morphology (Figure 7). We observed a decreasing average roughness size and increasing amount of defects (it is obvious from Figure 7).

After analysis we can say that the structure of defects changes on nanograin interfaces due to annealing, average roughness size decreases, and nanohardness increases by 20% (in comparison with as-deposited state), which correlates with our previous works [16,17]. Friction ratio decreases to 25%—it is the main difference as opposed to works [18–20].

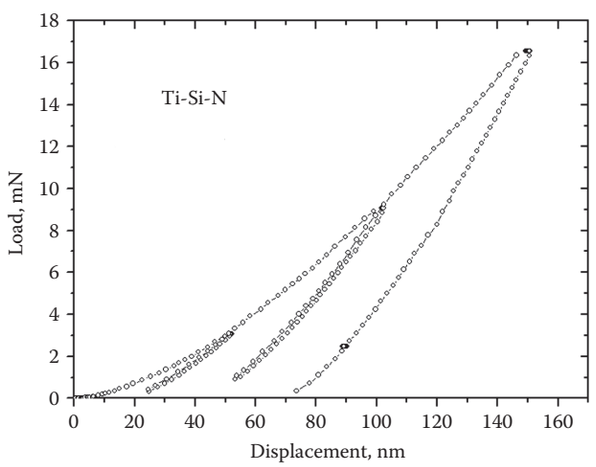

FIGURE 6 Loading and unloading curves, obtained for Ti–Si–N coating (U = –100 V, P_n = 0.7 Pa), indentation on 50, 100, and 150 nm depth.

INVESTIGATION OF ELEMENT PROFILES, DEFECTS, PHASE COMPOSITION, AND PHYSICAL AND MECHANICAL PROPERTIES OF SUPERHARD COATINGS TI–HF–SI–N

Before turning to the analysis of x-ray data, it should be noted that, for understanding of the sequence of processes occurring in the surface region during the deposition, it is necessary to compare the heat of formation of possible nitrides. In accordance with [23], $\Delta H298$ (HfN) = –369.3 kJ/mol, $\Delta H298$ (TiN) = –336.6 kJ/mol, $\Delta H298$ (Si_3N_4) = –738.1 kJ/mol. It means that the heat of formation of all systems is relatively large and negative, indicating that there is a high probability of the formation of such systems through the transfer of material from the target to the substrate. In this case, the proximity of the values of the heat formation of TiN and HfN creates conditions for the formation of sufficiently homogeneous solid solution (Ti, Hf)N.

Since the x-ray study indeed revealed the formation of this particular two-phase system (because the diffraction peaks of this phase are between peaks from mononitrides TiN [JCPDS 38-1420] and HfN [JCPDS 33-0592]), we identified this phase as a substitutional solid solution (Ti, Hf)N, and the diffused peaks of low intensity, which are present in the diffraction spectrum in the angular range of 2θ = 40°–60°, are apparently related to the spectrum peaks of the second α-Si_3N_4 phase (Figure 8, curve 3). Conditions of formation of

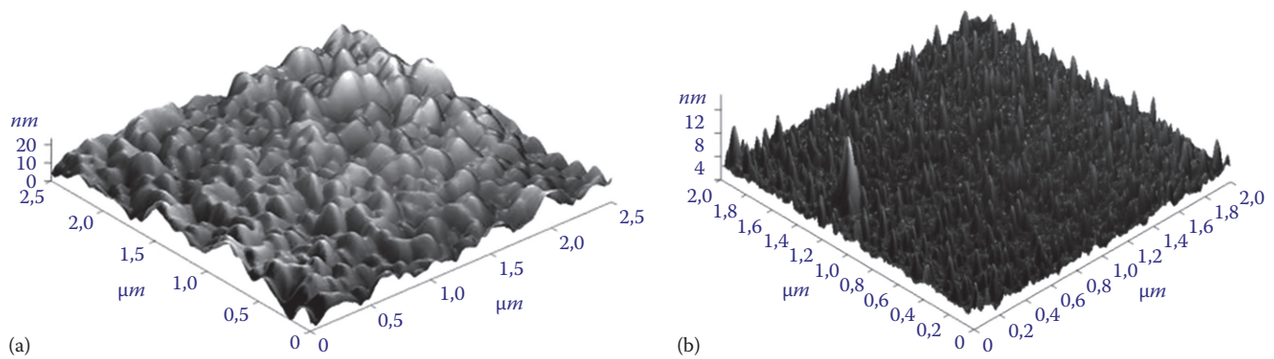

FIGURE 7 Ti–Si–N coating's surface morphology: (a) 3D AFM image and (b) after annealing under the temperature of 600°C.

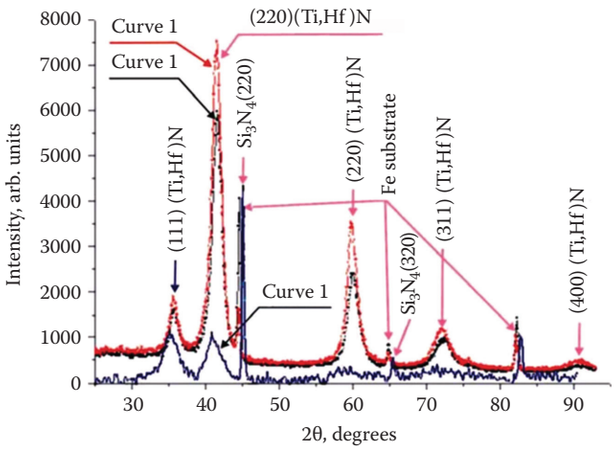

FIGURE 8 Diffraction spectra of Ti–Hf–Si–N coatings, obtained for the three series of samples.

nanocomposite coating Ti–Hf–Si–N lead to significant lattice strain of the crystallites, so in the coating the compressive stresses are occurring. Diffraction patterns shown in Figure 8 (curves 1 and 2), obtained by the separation of the ion-plasma flow, illustrate the definition of a crystal lattice deformation in sample series 3. In this case, we analyzed by imposing lines in the oblique mode (spectra) and determined that for sample series 3 (curve 1), the deformation $<\Sigma> = -1.9\%$, (lattice parameter $a = 0.4305$ nm) and for sample 11 of series 3 (curve 2), the deformation is $<\Sigma> = -1.6\%$ (the lattice parameter $a = 0.4303$ nm). Data analysis of x-ray diffraction shows that the coating obtained from the target of the same composition is very different from the characteristic structural features, depending on the separation or nonseparation (jet) beam. The results of this analysis are shown in Table 5.

Figure 9 shows that in the jet mode of the plasma flow without separation, the nontextured polycrystalline coatings with sufficiently high relative intensity of the peaks (the latter, at a comparable coating thickness, indicates a relatively high content in solid solution Hf, having a large reflectivity compared to Ti) are formed.

During the process of beam separation, the produced (deposited) coatings are differently textured. In case of supplying the substrate by low potential (–100 V) we get a texture with the [110]. Thus the structure of the coating is composed of textured and nontextured crystallites. The volume content of textured crystallites is about 40% of the total, and the lattice constant in comparison to nontextured crystallites increases. The most likely reason for this increase may be a nonuniform distribution of hafnium atoms in the coating with their primary content in the lattice of textured crystallites. Herewith the texturing leads to increase of the average crystallite size in the direction of the film-forming particle deposition (perpendicular to the growing surface). For example, in the fraction of

AQ8

TABLE 5
Results of Measurements of Tribomechanical Properties for Different Sample Series of Ti–Hf–Si–N Coatings

Sample Series	Friction Coefficient	Average Crystallite Size, nm	Hf Content in Solid Solution (Hf, Ti) Based on the Period Size, at%	Hardness, GPa	Stoichiometry of Series
1	0.25–0.2	6.7	19	42.7	Ti_{24}–Hf_{10}–Si_6–N_{60}
3	0.5–0.45	4.0	65	37.4	Ti_{33}–Hf_{29}–Si_{13}–N_{25}
	0.12–0.45	4.3	69	38.3	
1	0.3–0.6	5.0	33	44.6	Ti_{24}–Hf_{10}–Si_6–N_{60}
	0.5–0.45	3.9	45	39.7	
2	0.18–0.22	6.5	30	48.6	Ti_{24}–Hf_{14}–Si_{12}–N_{50}
	0.15–0.26	7	28	45.4	

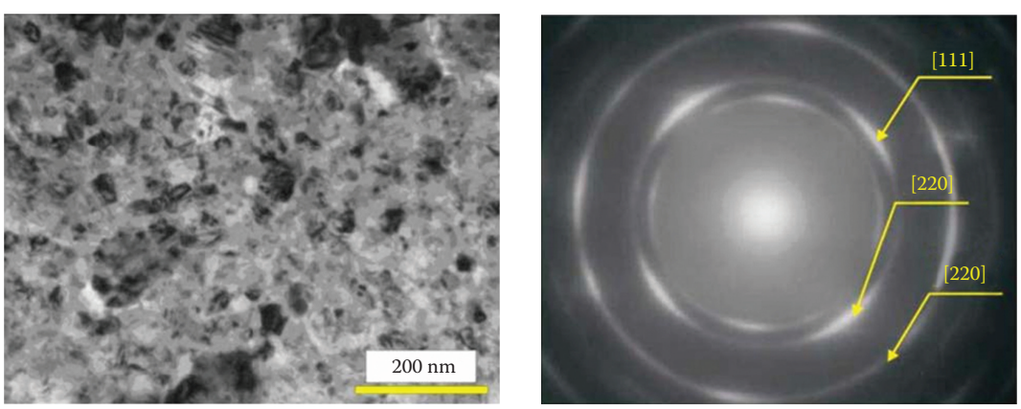

FIGURE 9 Images of structure areas of nanocomposite Ti–Hf–Si–N coating, obtained by TEM JEOL 2010 F: (a) structure of surface and (b) dark-field image of the nanograin structure.

nontextured crystallites, their average size is 6.7 nm, while in the fraction of textured crystallites, the size is much higher and is 10.6 nm. This type of coating is characterized by the highest value of nanohardness (see Table 5). In case of rising voltage up to −200 V and use of scheme with separation during the deposition, the coating is formed with reduced average crystallite size (to 5.0 nm) and the fraction of textured crystallites (less than 20 vol%) is also significantly reduced. Herewith, the axis texture is oriented as [001]. It should also be noted that the rising of accelerating voltage from −100 to −200 V (i.e., increasing energy of the plasma flow) leads to formation of textured factions with the same value of the spatial period. However, the magnitude of the lattice in this case exceeds a period of nontextured fraction formed when applying a low potential to the substrate and is 0.4337 nm. This period, assuming Vegard's rule for solid solutions, corresponds to the content of 33 at.% Hf in a metallic solid solution (Hf, Ti) of the nitride phase (in the calculation the tabulated values of periods are used: TiN = 0.424173 nm [JCPDS 38-1420] and HfN = 0.452534 nm [JCPDS 33-0592]) [8,29].

As it is known, the action of compressive stresses in the coating results in a reduction of the angle of the diffraction peak detected during the diffraction shooting by scheme θ–2θ, and the corresponding calculation leads to an overestimation of the value of the period, that is, to the overstate of the value of the Hf concentration in solid solution (the error may be 5–10 at.%). Therefore, the calculations made here can give the information only about the upper limit of the concentration of Hf in solid solution. All the aforementioned refer to the samples obtained at the typical pressure in the chamber at 0.6–0.7 Pa during the deposition process. In the case of reduction of pressure to 0.3 Pa, carried in the separation mode with a voltage of 200 V (series 1, No 31), an increase of the relative content of the heavier atoms of Hf in the coating is observed. In addition, during the reduction of pressure, the average size of the growing crystallites also decreases. The effects observed in this case can be associated with an increase in the radiation factor at low operating pressures. Indeed, lowering of the operating pressure must be accompanied by decrease of the probability of loss of energy by collision atoms in the *target–substrate* gap. Thus, maintaining a relatively high energy of deposition, the film-forming atoms on the substrate stimulate the processes of secondary sputtering and radiation defect-forming, which in the first case leads to increase of the relative content of Hf atoms in the coating and in the second case to increase of the nuclei number and, consequently, to the decrease of the average crystallite size in the coating. In the coatings obtained under a characteristic pressure, 0.6–0.7 Pa in the absence of beam separation (in ramjet mode), a higher value of the lattice parameters is realized, which is determined by increasing the content of Hf atoms (see Tables 2 and 5) [8]. Apparently, more intensive jet mode of deposition leads to decrease of the average crystallite size, the cause of which is the increasing density of nucleation at a time. In addition, a more pronounced effect of reducing the crystallite size can lead to the use of a larger voltage (–200 V), which is natural, since the increase of the radiation factor promotes the dispersion structure [32].

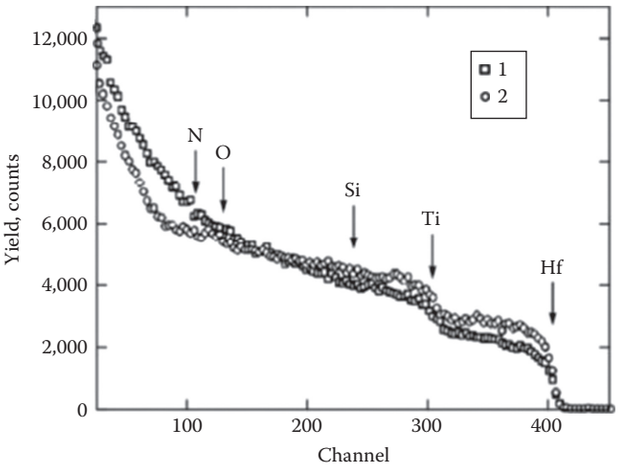

FIGURE 10 Energy spectra of RBS of He^+ ions with an energy of 1.3 MeV for samples of the steel with the Ti–Hf–Si–N film: (7) at a potential of 100 V, p = 0.6 Pa (first series of samples), and (2) at a potential of 200 V, p = 0.7 Pa (second series of samples). AQ9

Figure 10 presents the results obtained from the RBS investigation of the elemental composition of the superhard nanostructured Ti–Hf–Si–N films. It can be seen from this figure that, for the first series of samples with coatings (Figure 10, curve 1), the composition of the Ti–Hf–Si–N films is described by the formula $(Ti_{37}Hf_9Si_8)\ N_{46}$.

The concentration distribution profiles of elements over the depth of the Ti–Hf–Si–N coating, which correspond to the RBS spectra (Figure 10), are calculated under the assumption that the atomic density of the layer is close to the atomic density of TiN. It is well known that RBS is a reference method for determining the concentration of elements with a large atomic number, as well as for determining the thickness of the films.

Furthermore, it is a nondestructive method, and this property is its advantage. At the same time, SIMS is a more sensitive method of analysis (the detection limit is ~10−6 at.%) (Figure 11). Therefore, a comparison of the results obtained using the RBS, SIMS, and GDMS methods provides a more realistic picture of the distribution of the elemental composition of the coating over the depth of the layer. This has made it possible to analyze the composition of the film as a whole over the depth from the film surface to the film–substrate interface, including the determination of concentrations of oxygen and carbon uncontrollable impurities, which come from the residual atmosphere in the working chamber.

Figure 12a and b shows the energy-dispersive spectra obtained from the Ti–Hf–Si–N sample (series 1). Figure 12a is the integral information from the area of 2 × 2 mm, and Figure 12b shows information about local analysis. As can be seen from these spectra, there is no particular difference between them, which witnesses about the uniform distribution of the elements in depth of coating.

The test results on sample series 23 with the use of the REVETEST scratch tester are presented in Figure 13a. It should be noted that as the load on the indenter increases, the dependence of the friction coefficient on the load becomes

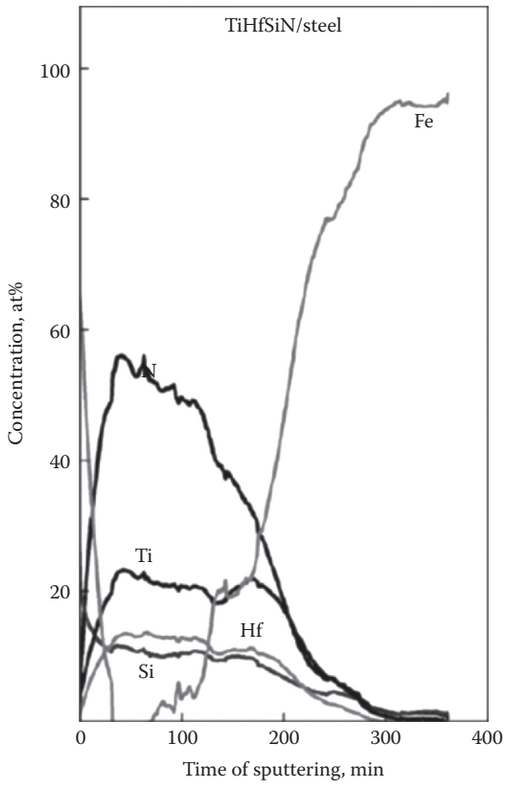

FIGURE 11 Concentration profiles of elements in the Ti–Hf–Si–N film according to the SIMS analysis for the first series of samples. The high Fe concentration is observed in the substrate material (steel).

oscillatory in character: an increase in the friction coefficient is accompanied by a sudden burst of acoustic emission and a retardation of penetration of the indenter into the material. This behavior of all the measured parameters indicates that the hard coating with a thickness larger than 1 μm on the surface of a softer material exhibits a significant resistance to the diamond indenter until it is completely abraded under large loads [30].

When testing the coating, we can clearly identify threshold values of the critical load, which lead to different types of fracture. The fracture of the coating begins with the emergence of individual chevron cracks at the bottom of the wear groove, which is responsible for the increase in local stresses and friction force. This leads to a rapid wear of the coating (Figure 13b).

In this work, two main critical loads were determined from the changes in the curves of the dependences of the friction coefficient and acoustic emission on the scribing load (Figure 13a). The first critical load corresponds to the onset of cohesive failure of the coating, whereas the second critical load corresponds to the plastic wear of the coating (adhesive failure). According to the results of adhesion tests, we can argue that the cohesive failure of sample series 23 occurs at a load of 2.38 N and its adhesive failure at a load of 9.81 N.

Figure 14 shows the dependence of *S*-parameters from the energy of the incident positron microbeam. Presented profiles of vacancy-type defects in the coating depth (series 2 [a] and series 3 [b]), significantly differ by the stoichiometry (content) of the elements and by the phase composition (Figure 9). It is seen from the figure, where the behavior of the curves differ markedly, that in the case of sample series 2, we have a two-phase system consisting of a-Si_3N_4 and (Ti, Hf)N. Namely, a two-phase coating is characterized by two peaks (increase *S*-parameter) in the region of 10 keV and then in the region of 20 keV (near the coating–substrate interface). In the case of sample series 3, we have a single-phase solid solution of (Ti, Hf)N and the *S*-parameter value is rather high, −0.492, and after reaching the film–substrate interface, it begins to decrease to a value of 0.476 [24–27].

Figure 15a through c shows the results of the wear resistance tests of samples 23 (a), 31 (b), and 35 (c). Based on the obtained data, it can be argued that the coating of series 23 (the smallest material removal, Figure 13a) with the lowest Hf content in solid solution (Ti, Hf)N (Table 2) has the greatest wear resistance. Accordingly, the degree of wear resistance decreases with increasing Hf content in the solid solution (Figure 13b and c).

Destruction of the coating begins with the appearance of individual chevron cracks at the bottom of the wear groove, resulting in the increase of the local stress and friction. This leads to rapid subsequent abrasion of the coating.

According to the results of adhesive tests of coating 23, cohesive destruction occurs at the minimum (critical) load L_{C1} = 2.38 H, and adhesive destruction (plastic wear) comes with a load of the first crack appearance L_{C2} = 9.81 H.

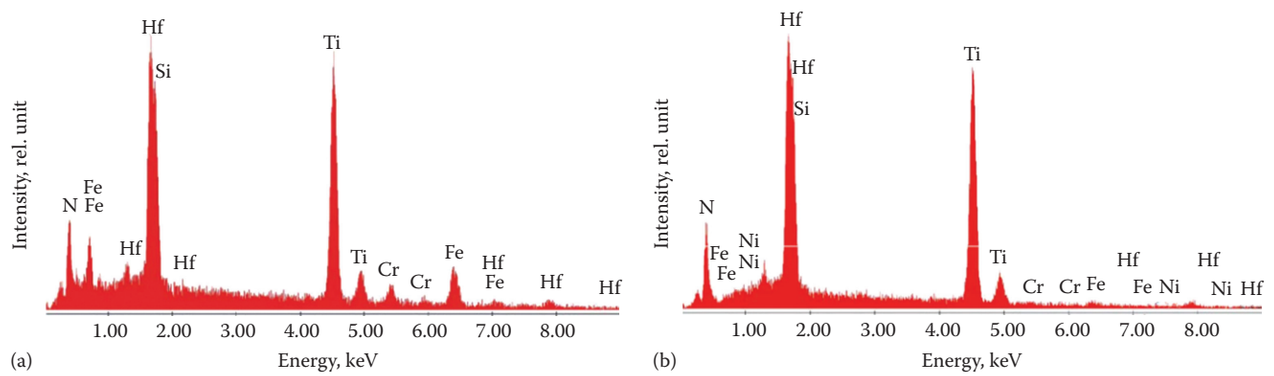

FIGURE 12 (a), (b) Energy-dispersive spectra of samples with Ti–Hf–Si–N coatings (series 1): (a) integral information from area 2 × 2 mm and (b) local analysis.

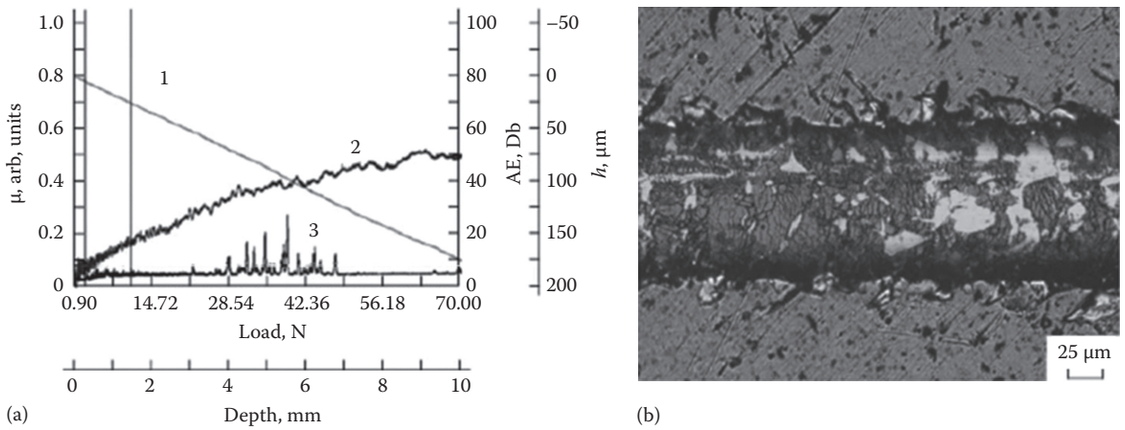

AQ10 **FIGURE 13** Results of adhesion tests of the Ti–Hf–Si–N coating/steel substrate system for sample series 23: (a) (1) the penetration depth *h*, (2) the friction coefficient μ, and (3) the acoustic emission (AE) and (b) the structure of the coating in the fracture zone at loads in the range of 0.9–90.0 N.

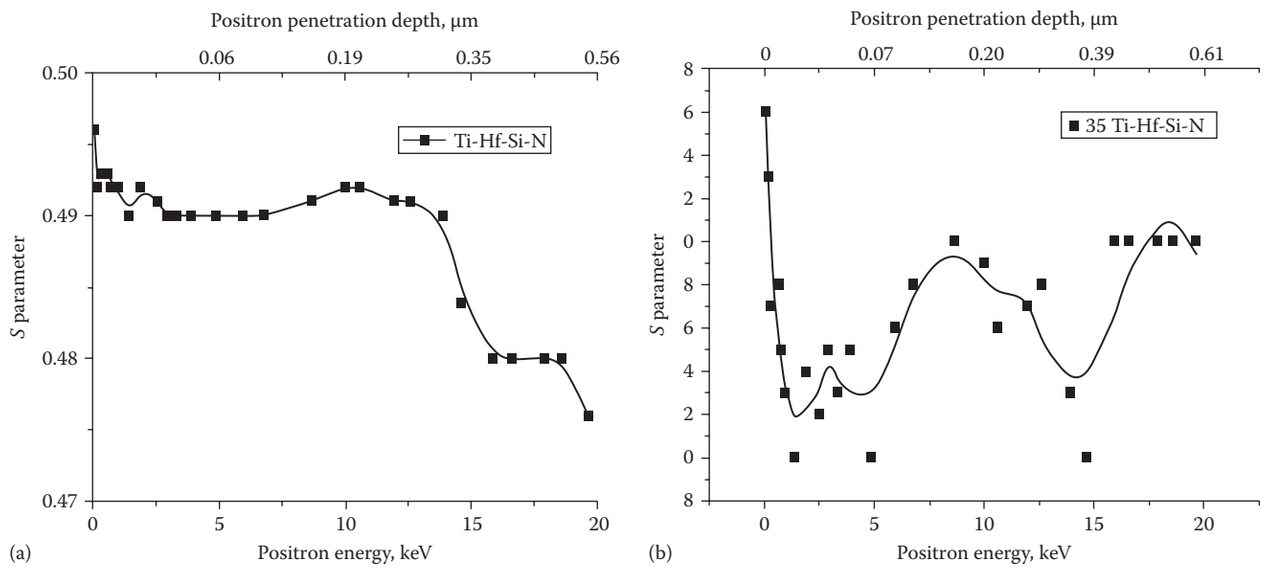

FIGURE 14 The dependence of the *S*-parameter on the incident positron microbeam energy of sample series 2 (a) and series 3 (b).

The friction coefficient of sample 35 in the initial stage is 0.15, at the next stage, after 2.5 m of friction of the coating is destroyed (potholes and cracks are appearing). The friction coefficient increases to 0.45, which confirms not very high hardness of the coating. In case of testing of the next coating sample (sample 23), the friction coefficient increases up to 0.25 due to the high roughness of the coating, and when the steady depreciation stage is set, the friction coefficient reaches the value of 0.2. A detailed study of parameters such as the friction coefficient, acoustic emission, and penetration depth of the indenter was performed for all samples [30–33].

So finally we can state that new superhard nanostructured coatings (films) based on Ti–Hf–Si–N with high physical and mechanical characteristics and different stoichiometries (depending on the deposition conditions) have been fabricated. It has been found that a decrease in the size of nc-(Ti, Hf)N nanograins from 6.7 to 5.0 nm and the formation of the α-Si_3N_4 phase (in the form of an amorphous or quasi-amorphous interlayer between the nanograins) result in an increase in the nanohardness from 42.7 to 48.4 ± 1.4 GPa. It has been established that, with an increase in the accelerating voltage to –200 V (separated and nonseparated beams) during the deposition, the coatings with a smaller average crystallite size (up to 5.0 nm) are formed on the substrate. An increase in the accelerating voltage from –100 to –200 V leads to the same value of the lattice parameter for both the textured and nontextured factions. In the case where the pressure decreases to 0.3 Pa, the relative content of Hf atoms in the coating increases and the average size of growing crystallites decreases.

Thus, the adhesion and tribological tests have made it possible to determine the adhesive strength, friction coefficient, and deformation characteristics of the Ti–Hf–Si–N

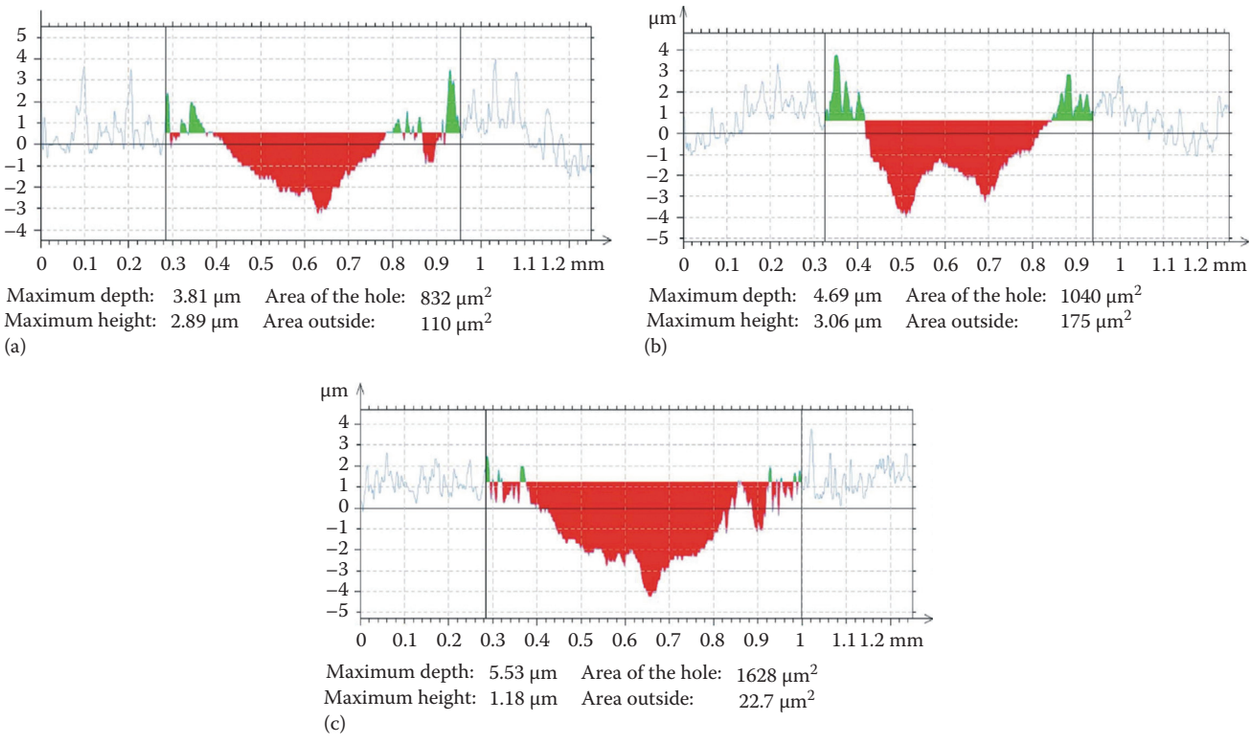

FIGURE 15 (a) through (c) The results of wear resistance tests on the scratch tester REVETEST of samples (a) 23, (b) 31, and (c) 35.

coatings on the steel substrate. Based on measurements of different physical parameters during the adhesion tests, the processes of elastic and plastic deformations in the coating/substrate system have been described, and the threshold values of the critical load leading to different (cohesive and adhesive) types of failure of the coatings have been determined. The synthesized coatings have high values of hardness, wear resistance, and adhesion to the substrate and low values of the modulus of elasticity and friction coefficient, which makes them promising thin-film materials for use in mechanical engineering.

EFFECT OF THERMAL ANNEALING IN VACUUM AND IN AIR ON NANOGRAIN SIZES IN HARD AND SUPERHARD COATINGS Zr–Ti–Si–N

Analyzing the phase composition of Zr–Ti–Si–N films, we found that a basic crystalline component of as-deposited state was a solid solution (Zr, Ti)N based on the cubic lattice of a structured NaCl.

Crystallites of solid (Zr, Ti)N solution underwent compressing elastic macrostresses occurring in a *film–substrate* system. Compressing stresses, which were present in a plane of growing film, indicated the development of compressing deformation in a crystal lattice, which was identified by a shift of diffraction lines in the process of angular surveys ("$\sin^2\psi$–method") and reached −2.93% value. With $E \approx 400$ GPa characteristic elastic modulus and 0.28 Poisson ratio, the deformation value corresponded to that occurring under the action of compressing stresses $\sigma_c \approx 8.5$ GPa.

Figure 16 shows the morphology of the surface on (Zr–Ti–Si)N base formed with $U = -150$ V, $P = 0.8$ Pa. Investigated, that a change in direction of increasing the potential applied to the substrate, the roughness decreases [34]. AQ11

The resulting coatings have the following hardness: TiN ($H = 28$ GPa and $E = 312$ GPa); Ti–Si–N ($H = 38$–39 GPa, $E = 356$ GPa); Ti–Zr–Si–N hardness values $H = 38\ldots41$ GPa; and $E = 478$ GPa. Tables 6 and 7 show the results of tribological tests.

The chamber pressure is an insignificant effect on the morphology, but it is noted that the increase in gas pressure in the chamber leads to a decrease in surface roughness, the optimal parameters of the chamber pressure, and the potential applied to the substrate ($U = -150$ V, $P = 0.8$ Pa) under which the maximum peak is 16 nm.

We should also note that such high stresses characterize nitride films, which were formed under deposition with a high radiation factor, which provided high adhesion to the base material and development of compression stresses in the film, which was stiffly bound to the base material due to the "atomic peening" effect [35–41].

At sliding speeds, 10 cm/s is a normal abrasive oxidative wear friction. The structural-phase state coverings play a crucial role in the processes of wear and temperature dependent. At temperatures of 30°C, tests are covering adhesive interaction with the counterbody—there is a rough surface topography of the coating. At temperatures of 300°C, tests for coatings based on Ti–Si–N and Zr–Ti–Si–N coating decrease the wear and the wear counterface increases. With further increase in temperature to 500°C, the wear coating

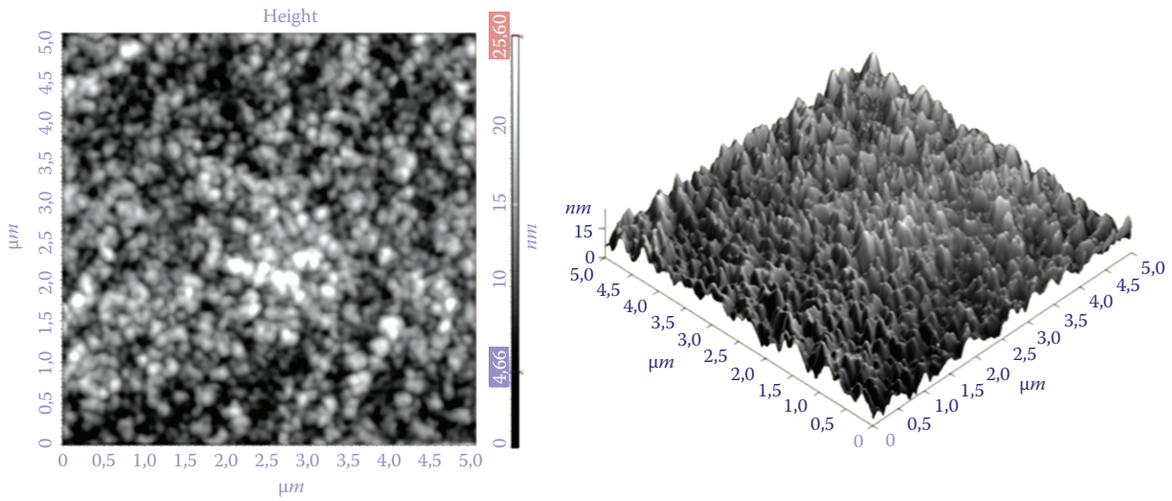

FIGURE 16 Surface morphology of coatings on (Zr–Ti–Si)N base with $U = -150$ V, $P = 0.8$ Pa.

TABLE 6
Results of Tribological Properties of Nanocomposite Coatings

Coatings	Temperature Tests,°C	Wear Coating Factor, mm³/nm	Wear Factor of the Sample, mm³/nm	f_{mp}
Ti–Zr–Si–N	30	7.59×10^{-5}	1.93×10^{-5}	0.80
	300	2.22×10^{-5}	3.14×10^{-5}	0.71
	500	1.49×10^{-5}	2.81×10^{-5}	0.58
Ti–Zr–Si–N (a)	30	7.559×10^{-5}	3.214×10^{-5}	0.805
Ti = 22.73, Zr = 2.12, Si = 3.05	300	1.84×10^{-5}	4.726×10^{-5}	0.836
	500	1.47×10^{-5}	3.047×10^{-5}	0.582
Ti–Zr–Si–N (b)	30	6.75×10^{-5}	3.304×10^{-5}	0.793
Ti = 28.32, Zr = 2.67, Si = 3,64	300	3.62×10^{-5}	3.83×10^{-5}	0.813
	500	1.985×10^{-5}	2.749×10^{-5}	0.585
Ti–Zr–Si–N (c)	30	7.697×10^{-5}	3.279×10^{-5}	0.877
Ti = 27.46, Zr = 2.51, Si = 3.76	300	2.635×10^{-5}	3.486×10^{-5}	0.825
	500	1.955×10^{-5}	2.749×10^{-5}	0.632
Ti–Si–N	30	7.69×10^{-5}	3.28×10^{-5}	0.88
	300	2.63×10^{-5}	3.49×10^{-5}	0.82
	500	1.95×10^{-5}	2.75×10^{-5}	0.69
Ti–N	30	6.75×10^{-5}	3.30×10^{-5}	0.81
	300	3.62×10^{-5}	3.51×10^{-5}	0.87
	500	5.16×10^{-5}	3.83×10^{-5}	0.91

of Ti–Si–N and Zr–Ti–Si–N decreases, and their durability increases. This leads to a change in the conditions of the processes occurring in the contact zone due to changes in the structure of surface layers.

Qualitative changing of phase composition was observed in films under vacuum annealing at $T_{an} > 1000$°C. Appearance of zirconium and titanium oxides was related to oxidation relaxation under coating surface interaction with oxygen atoms coming from residual vacuum atmosphere under annealing.

Figure 17 shows that the results of RBS analysis on the samples obtained were coated with Ti–Zr–Si–N. The beam energy of He ions is not sufficient for the analysis of the total film thickness, but the peaks of Ti and Zr are well separated and can be seen that the concentration of Ti and Zr is almost uniformly distributed over the depth of coating [39–41].

But still, Si concentration was not less than 7 at.%, while that of N might reach more than 15 at.%. Figure 18 shows the scratch properties of Zr–Ti–Si–N. The friction coefficient (μ) between two solid surfaces is defined as the ratio of the tangential force (F) required producing sliding divided by the normal force between the surfaces (N). Normal force F_n (occasionally N) is the component, perpendicular to the surface of contact, of the contact force exerted on an object by the surface. Acoustic emission is a naturally occurring phenomenon whereby external stimuli, such as mechanical loading, generate sources of elastic waves. Penetration depth

TABLE 7
Macrostructure of the Surface of the Nanocomposite Coatings Ti–Zr–Si–N

Options	$T = 30°C$	$T = 300°C$	$T = 500°C$
Sample	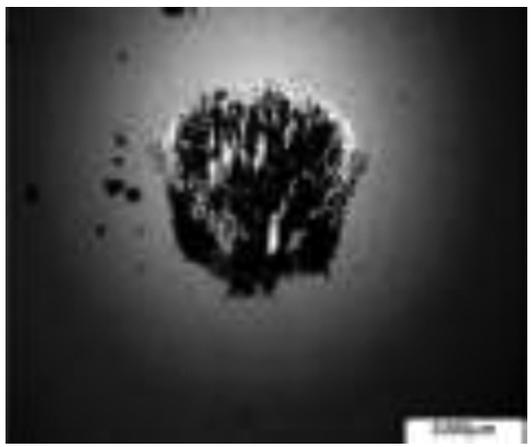	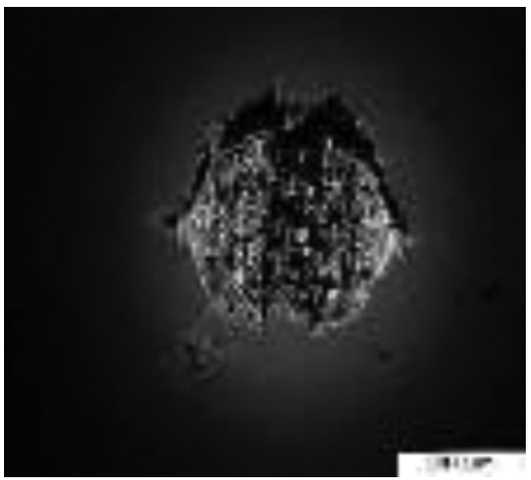	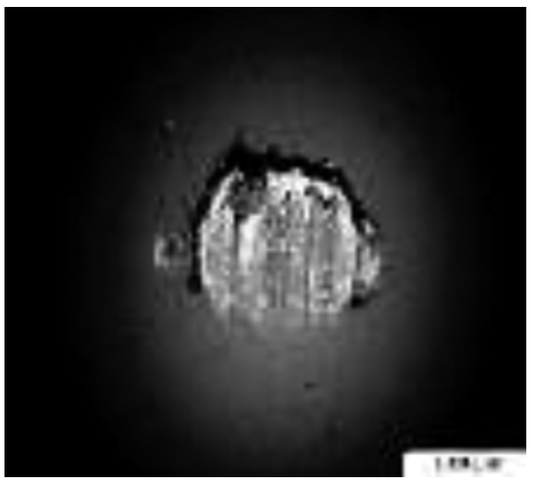
Friction track	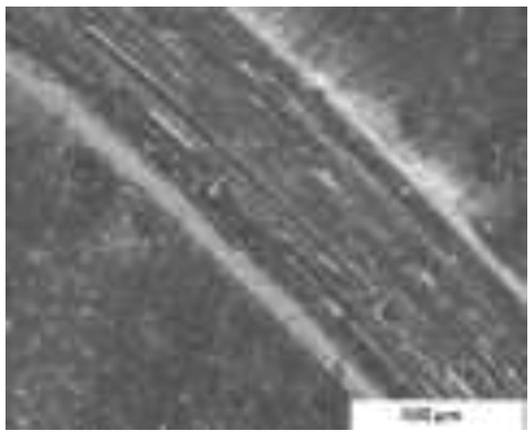	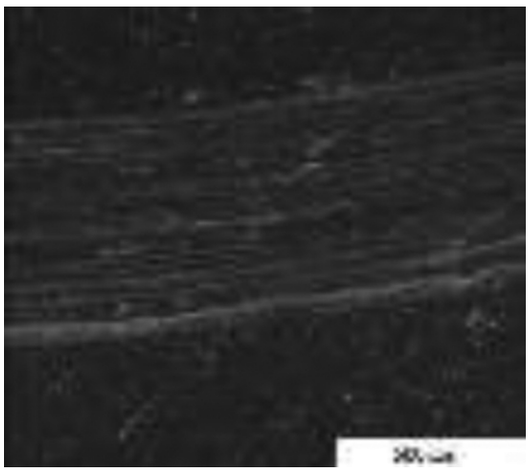	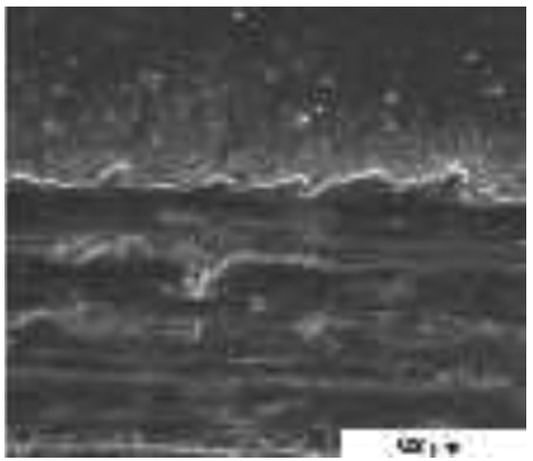

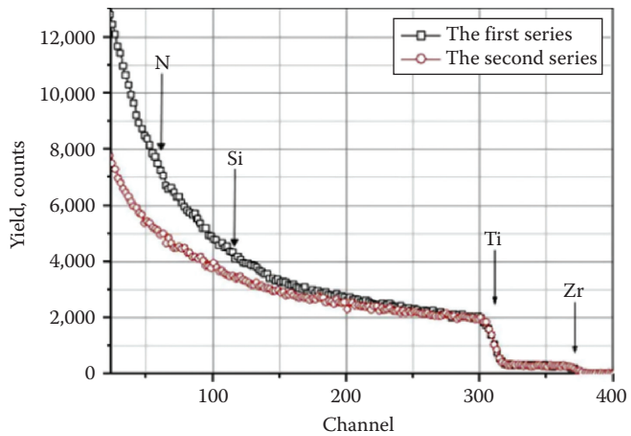

FIGURE 17 Energy spectra of Rutherford ion backscattering (RBS) for thin coating Zr–Ti–Si–N.

is a measure of how deep light or any electromagnetic radiation can penetrate into a material. It is defined as the depth at which the intensity of the radiation inside the material falls to $1/e$ (about 37%) of its original value at (or more properly, just beneath) the surface.

Under annealing temperatures below 1000°C, coating phase composition remained practically unchanged. One could not only change width of diffraction lines and their shift to higher diffraction angles. The latter characterizes relaxation of compressing stresses in coatings. Changed diffraction lines were related to increased crystalline sizes (in general) and decreased microdeformation.

Three-dimensional islands on the surface of the films with columnar structure are output on the surface of the ends of individual grains (Figure 19). It is seen that the roughness depends on the conditions of their chemical composition and the parameters of the wasp assertion. Undulation surfaces are associated with the mechanism of

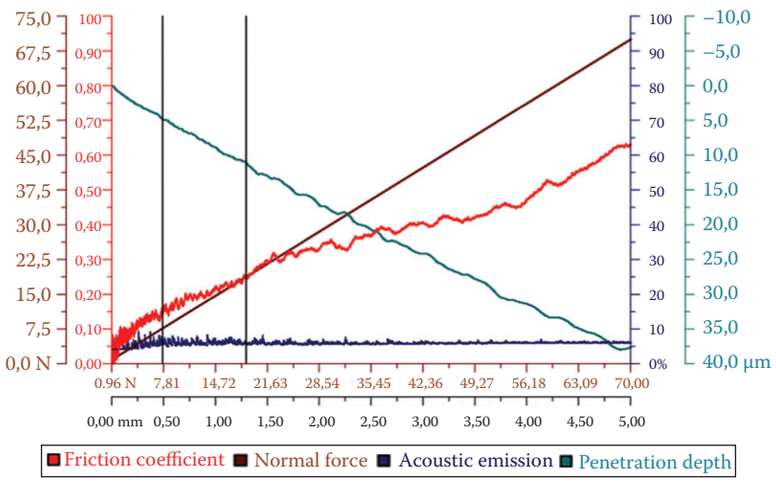

FIGURE 18 Scratch properties of Zr–Ti–Si–N: friction coefficient, normal force, acoustic emission, penetration depth.

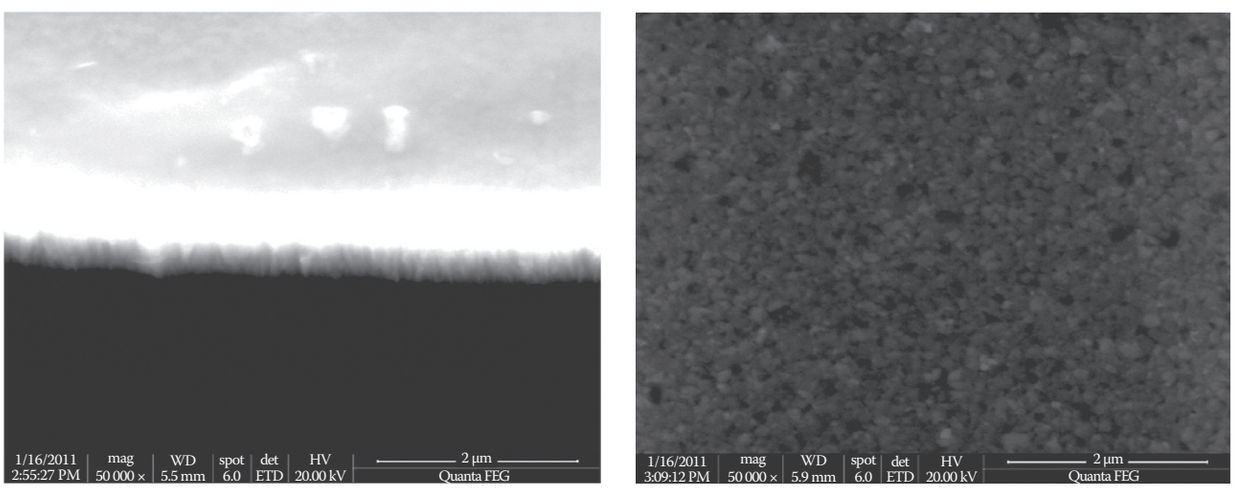

(a) (b)

FIGURE 19 Coating Ti–Zr–Si–N with a columnar structure: (a) a cross section of the coating and (b) surface topography of the coating.

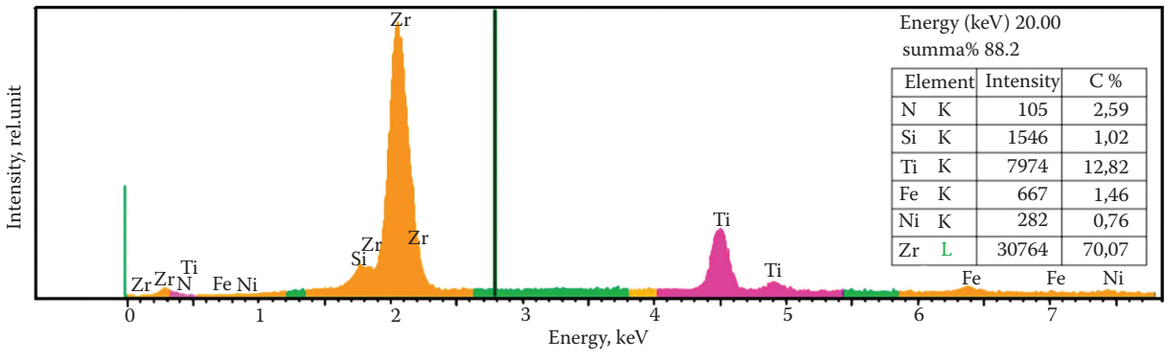

FIGURE 20 Data of microanalysis for point of Zr–Ti–Si–N (Ti ≈ 12%) nanocomposite coating surface (fifth series).

growth, with the formation of separate islands on the surface (Volmer–Weber mechanism) [39,40].

In such a way, hardness, which was increased in the process of annealing, seems to be related to incomplete spinodal phase segregation at grain boundaries resulting from deposition of Zr–Ti–Si–N–(nanocomposite). Annealing stimulated spinodal phase segregation, forming more stable modulated film structures.

Figure 20 shows the chemical composition over coating cross section. Spectra indicate that N concentration changed from 3.16 to 4.22 wt.%, Si concentration was about 0.98 to 1.03 wt.%, Ti was 11.78 to 13.52 wt.%, and Zr = 73.90 to 77.91 wt.%. These results indicated that the amount of N is essentially high, and this allowed it to participate in the formation of nitrides with Zr, Ti, or (Zr, Ti)N solid solution. Si concentration was low; however, results reported by Veprek et al. indicated Si concentration as high as 6–7 at.%, which was enough to form siliconitride phases.

Changes occurred under macrodeformation of crystallites of basic film phase—(Zr, Ti)N solid solution. Compressing deformation of crystallite lattices increased, which seemed to be related to additional new crystalline components, which appeared in film material: oxides and siliconitrides. In the lattice itself, a period decreased corresponding to increased Ti concentration. Ordered atoms in metallic (Zr/Ti) sublattice of solid solution increased from 8.5 to 21 at.%.

In this temperature range, crystallite size increased from 15 to 25 nm, crystallite lattice microdeformation increasing nonessentially up 0.5%–0.8%. Table 8 summarizes the substructure characteristics of (Zr, Ti)N solid solution crystallites.

In comparison with vacuum annealing, air is characterized by a decrease of phase stability above 500°C–600°C. Above these temperatures, one observes the formation of oxides resulting in film destruction and total film destruction at 830°C.

Processes occurring in the film under annealing temperature below 600°C were similar to those occurring under vacuum annealing under the same temperature interval: they were characterized by decreased lattice period and lower values of micro- and macrodeformations accompanied by increasing concentration of deformation packing defects in the metallic sublattice of the solid solution.

Qualitative changing of phase composition was observed in films under vacuum annealing at $T_{an} > 1000$°C. Figure 21 shows a characteristic diffraction curve, which was taken under 30 min annealing at $T_{an} = 1100$°C. Under high-temperature annealing, in addition to (Zr, Ti)N nitrides (which period was close to ZrN lattice) and (Ti, Z)N (which period was close to TiN lattice), we observed diffraction peaks from zirconium oxide crystallites (ZrO_2, according to JCPDS Powder Diffraction Cards, International Center for Diffraction Data 42-1164, hexagonal lattice) and titanium oxide (TiO, JCPDS 43-1296, cubic lattice), and, probably, initial amorphous β-Si_3N_4 phase crystallites (JCPDS 33-1160, hexagonal lattice). Appearance of zirconium and titanium oxides was related to oxidation relaxation under coating

TABLE 8
Changes of Structure and Substructure Parameters Occurring in Ion-Plasma Deposited Coatings of the Zr–Ti–Si–N System in the Course of High-Temperature Annealing in Vacuum and in Air

Parameters of Structure	After Deposition	T_{an} = 300°C, Vacuum	T_{an} = 500°C, Vacuum	T_{an} = 800°C, Vacuum	T_{an} = 1100°C, Vacuum	T_{an} = 300°C, Air	T_{an} = 500°C, Air
*a*0, nm	0.45520	0.45226	0.45149	0.45120	0.45064	0.45315	0.45195
ε, %	−2.93	−2.40	−1.82	−1.01	−1.09	−2.15	−1.55
<ε″/, %	1.4	1.0	0.85	0.5	0.8	0.95	0.88
εdef. pack.	0.057	0.085	0.107	0.155	0.150	0.090	0.128

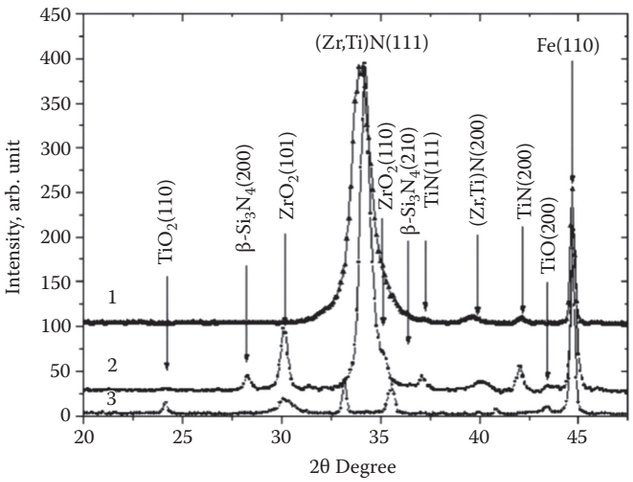

FIGURE 21 (1) Region of x-ray diffraction spectra taken for the condensates of the Zr–Ti–Si–N system after deposition; (2) after 30 min annealing in vacuum, under T_{an} = 1180°C; and (3) under T_{an} = 800°C in air. Three peaks, which are not designated in the curve, are for an oxide of the Fe_2O_3 substrate (JCPDS 33-0664).

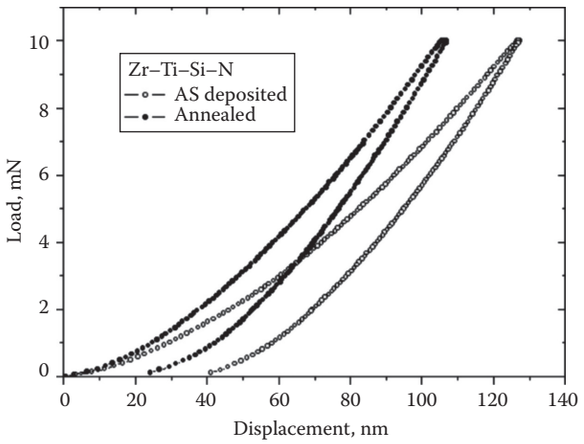

FIGURE 22 Load–displacement curves for as-deposited and annealed (500°C) Zr–Ti–Si–N effect of 500°C annealing in vacuum on nanohardness.

TABLE 9
Changes of Hardness and Elastic Modulus in Nanocomposite Coating before and after Annealing

Parameters	After Deposition	T_{an} = 300°C, Vacuum	T_{an} = 500°C, Vacuum
H, GPa	40.8 ± 2	43.7 ± 4	48.6 ± 6
E, GPa	392 ± 26	424 ± 56	456 ± 78

surface interaction with oxygen atoms coming from residual vacuum atmosphere under annealing.

In solid solution, hardness increased due to increasing Ti concentration and appearance of the Si_3N_4 phase. In the initial state, after deposition of those samples, with phase composition including three phases ((Zr,Ti)N-nc, ZrN-nc, and α-Si_3N_4), hardness was H = 40.6 ± 4 GPa and E = 392 ± 26 GPa. Annealing at 500°C increased H and E and decreased spread in hardness values, for example, H = 48 ± 6 GPa and E = (456 ± 78GPa) (see Table 9).

X-ray scanning method demonstrated a shift and broadening of diffraction peaks. The highest content of packing defects indicated a shift of most closely packed planes in a face-centered cubic (FCC) sublattice (111) with respect to each other and became pronounced under vacuum annealing at T_{an} = 800°C–1100°C reaching 15.5 vol.%. As it is seen from *loading–unloading* curves and calculation results, under annealing in vacuum at 500°C, nanohardness of Zr–Ti–Si–N films was H = 46 GPa (dark circles).

When Ti and Si concentration increased and three phases (nc–Zr–N, (Zr, Ti)N-nc, and α-Si_3N_4) were formed, average hardness increased to 40.8 ± 4 GPa. Figure 22 shows that in the initial state, the Zr–Ti–Si–N film (as received) had 40.8 GPa nanohardness. After annealing (a dark dotted curve) at 500°C in vacuum, coating nanohardness reached H = 55.3 GPa [32,38,40].

STRUCTURE AND PROPERTIES OF NANOSTRUCTURED (Ti–Hf–Zr–V–Nb)N COATINGS

The (Ti, Hf, Zr, V, Nb)N coating had an FCC crystal structure rather than coexisting separated nitrides. TiN, Hf N, ZrN, VN, and NbN had an FCC structure. Thus, the (Ti, Hf, Zr, V, Nb)N coating also exhibited an FCC solid solution structure, in which the Ti, Hf, Zr, V, and Nb atoms were randomly distributed over the metal sublattice. The same phenomena were also reported for as-deposited mixtures of FCC forming multiprincipal nitride elements such as AlCrTsTiZr [59], AlCrNbSiTiV [60], and TiVCrZrY [61]. This result not only implied the formation of a solid solution from all constituted nitrides but also confirmed the effect of high mixing entropy on the simplification of the crystal structure.

The solid solution phase with an FCC structure was also thermodynamically stable because it did not decompose or form other compounds even during annealing up to 873 K for 30 min. The stability of the FCC solid solution phase was also due to the high entropy effect. In addition, as shown in the chapter, the crystal size and lattice constant are shown.

Based on RBS, EDX, and XRD information, the composition variation and phase separation can be excluded since the composition and structures of coating hardly had any change. The stress relaxation of as-deposited coatings after annealing has been noted from a shift in the XRD peak position. This finding is attributed to the diffusion of implanted atoms to the surface, hence the annihilation of the stress-inducing defects, as will be shown using results of measurement of Doppler broadening of the annihilated peak (DBAP) of slow positron beam. Accordingly, the lattice decline was believed to result from a release of intrinsic microstress.

The morphology of coating surfaces and the element distribution were studied using the SEM with EDS analysis JEOL-7000 F.

Figure 23a shows the distribution of elements on the surface of samples in elemental contrast. Integrated analysis was obtained from the area of 0.1 mm × 10 mm. The intensity of the color indicates the concentration of elements. The dark spots on the surface of coating are the drop fraction, which appeared during the deposition of coating. Figure 23b and c shows the microanalysis results (EDX) of coatings obtained under different deposition conditions, and Figure 23d shows results of microanalysis after annealing at 873°K (for 30 min, at 100 Pa pressure in chamber).

As you can see from these results, the element concentration in the coating is N = 49.05 at.%, Ti = 22.92 at.%, V = 5.04 at.%, Zr = 6.84 at.%, Nb = 7.47 at.%, and Hf = 8.68 at.% at 2×10^{-2} Pa pressure. When the pressure decreases to 3×10^{-2} Pa, the spectra indicate a reduction of the specific content of the nitrogen atoms in the coating composition to N = 36.04 at.%, Ti = 20.13 at.%, V = 2.28 at.%, Zr = 17.12 at.%, Nb = 17.50 at.%, and Hf = $^{6.93}$ at.%. It means a significant deficiency of nitrogen atoms in nitrides of the multicomponent systems in comparison with stoichiometric ones at high pressure, 3×10^{-2} Pa. The results of RBS (Figure 24a and b) and EDX analyses indicate a crucial effect of the radiation factor (achieved by increasing of negative bias potential applied to the substrate) on segregation processes arising during the coating deposition. In other words, the energy of ion plasma flux increases due to the rising bias potential, which enhances the contribution of the radiation factor. It is known that the formation of a two-phase nanostructured film requires two terms: (1) the increased rate of atomic diffusion along the grain interfaces and (2) the high temperature of 873°K in the process of deposition to complete the process of spinodal segregation [45,46,53].

From the results of EDX analysis (see Figure 23d) after annealing of coatings, an oxide film is forming on the surface. It is also confirmed by XRD analysis of this sample presented in Figure 27b. The appearance of elements Fe and Cr on EDX spectra can be explained by diffusion of these elements from the substrate (which is made of steel). The deviation of the values of N concentration in coatings was not more than 0.26 at.% for coating with a concentration of N = 49.05 at.% and not more than 0.18 at.% for coatings with a concentration of N = 36.05 at.%. PAS experiments demonstrated that positrons are well localized in the areas of low electron density (i.e., vacancy-type defect divacancies, conglomerates of various vacancies, vacancy complexes, plus two or three interstitial atoms [53–56]). As it follows from Refs. [10,54–58], the nanostructured materials, fabricated using the compaction, are good traps for positrons, which then annihilate with two or three components of the positron lifetime τ_2, τ_3. It is associated with positron annihilation at the grain interfaces, that is, the quasi-amorphous phase, in our case. The presented results

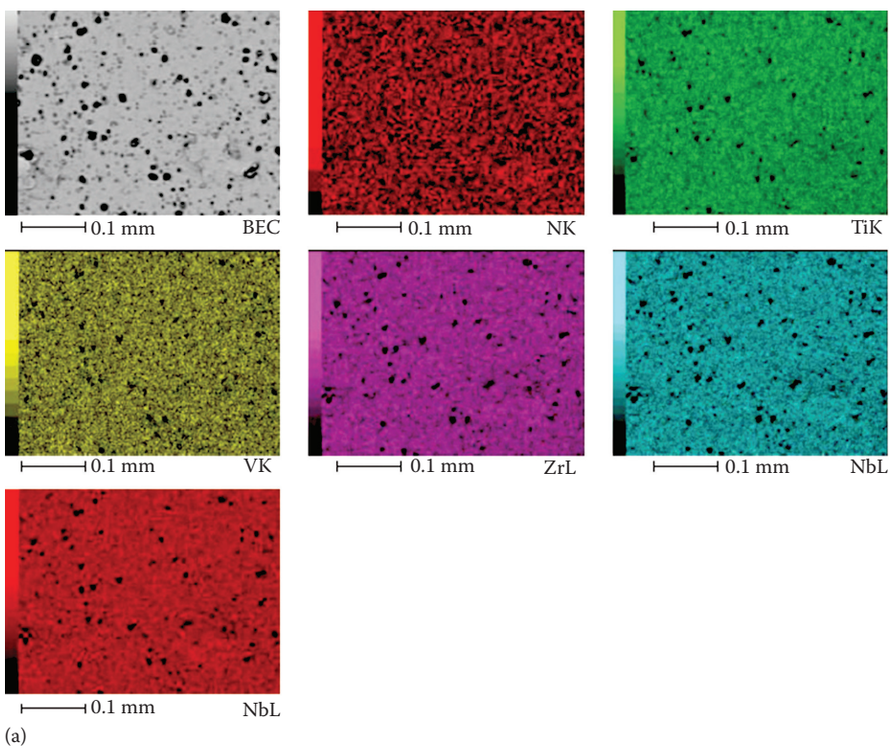

FIGURE 23 Images obtained by the scanning microscope JEOL-7000 F: (a) is the coating surface in reflected electrons; (*Continued*)

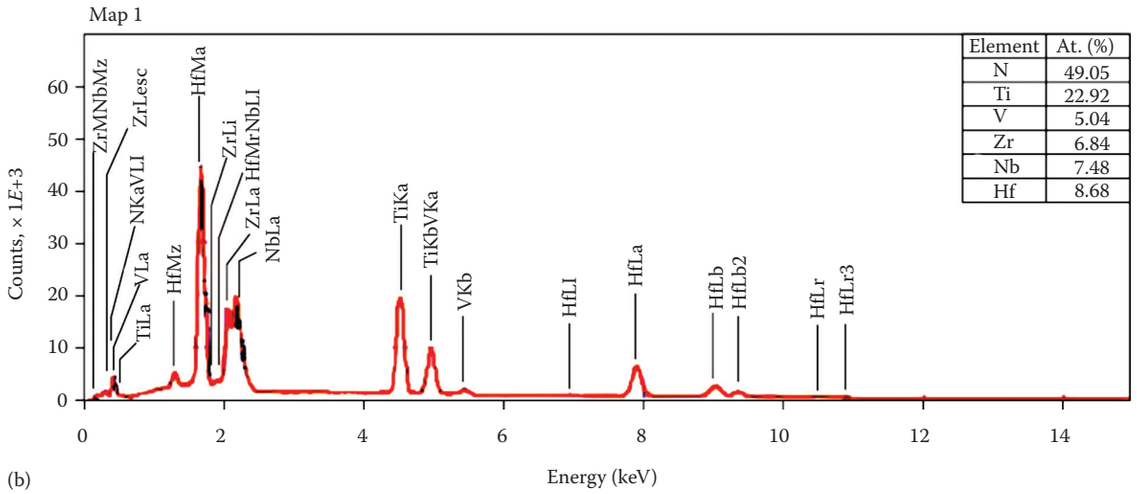

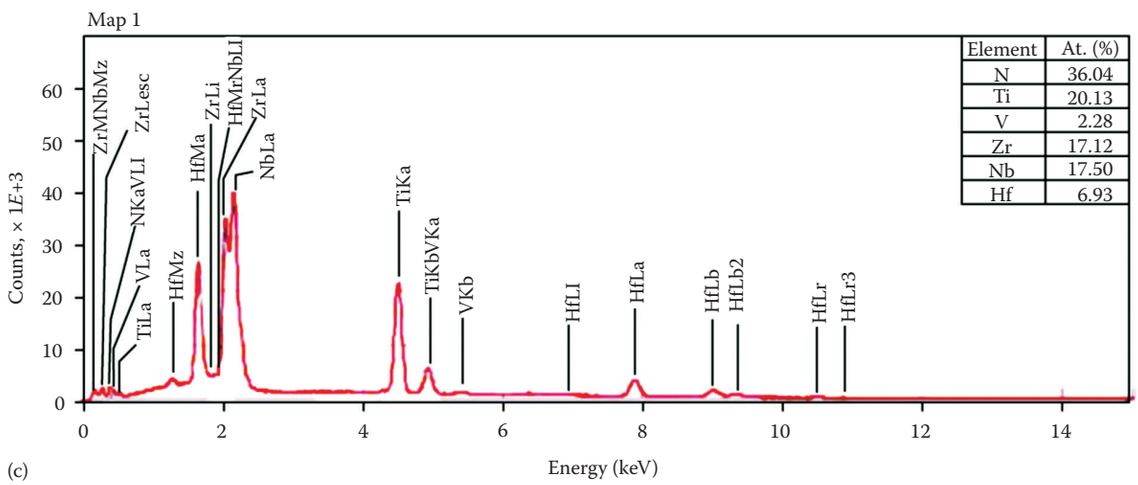

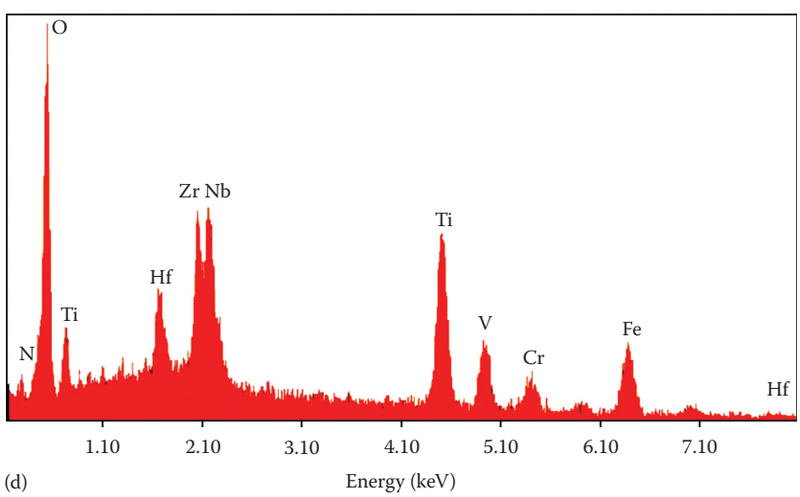

FIGURE 23 (*Continued*) Images obtained by the scanning microscope JEOL-7000 F: (b) shows microanalysis of coatings, N, Ti, V, Zr, and Nb, obtained under U_{bias} = –100 V, pressure $P = 2 \times 10^{-2}$; (c) shows microanalysis of coatings, N, Ti, V, Zr, and Nb, obtained under U_{bias} = –200 V, pressure $P = 3 \times 10^{-2}$; (d) shows microanalysis of coatings, N, Ti, V, Zr, and Nb after annealing at 873 K (for 30 min, at 100 Pa pressure in chamber).

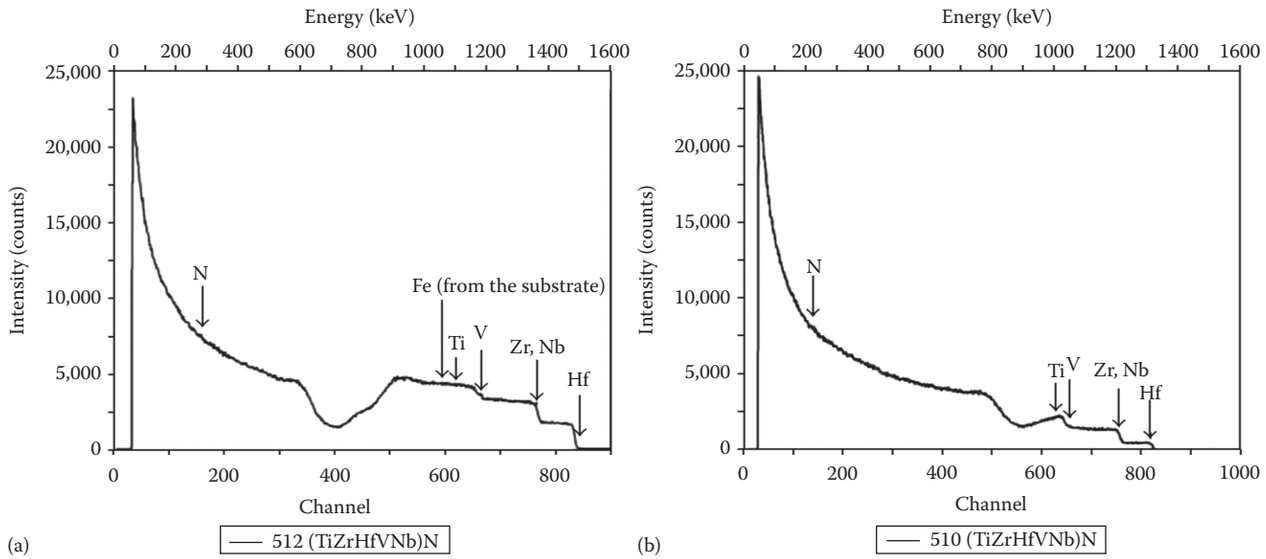

FIGURE 24 Results of the analysis of RBS spectra from samples 512 (a) and 510 (b).

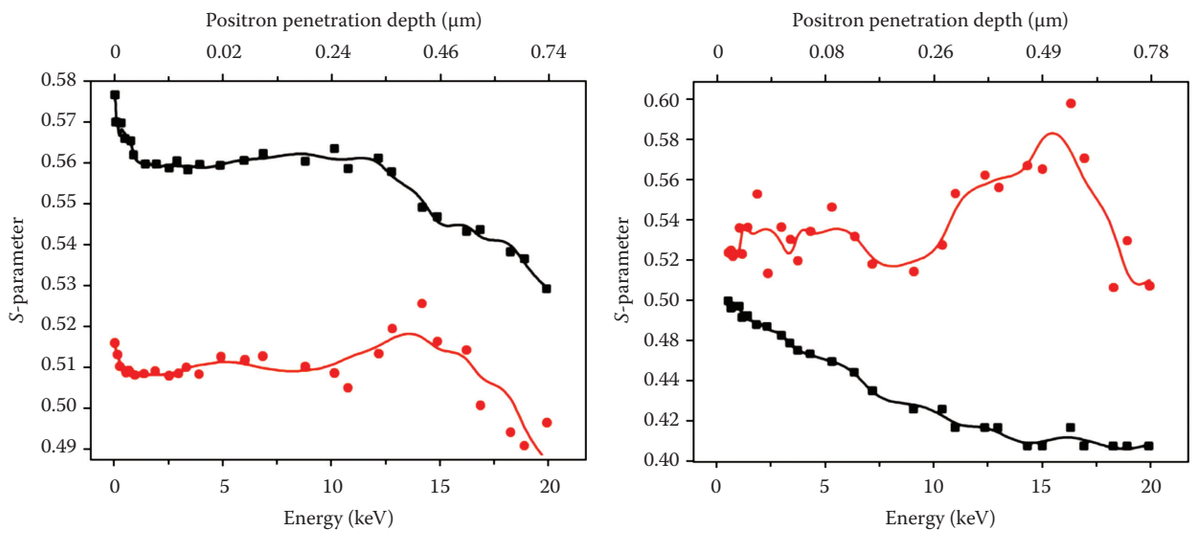

FIGURE 25 Dependencies of the *S*-parameter of the annihilation peak Doppler broadening measured over (Ti–Zr–Hf–V–Nb)N coating depth, for samples 512 (a) and 510 (b), after deposition and annealing at 873 K (100 Pa).

(Figure 25a and b) clearly indicate that the defect profiles (*S*-parameter) significantly differ for various deposition conditions; see, for example, samples 510 and 512. At the same time, thermal annealing in a chamber with a high enough residual pressure (100 Pa) leads to even greater changes of the *S*-parameter over the coating depth. The value of the *S*-parameter for sample 512 decreases from 0.58–0.56 to 0.52–0.51 after annealing, and only when the analyzing energy of positrons approaches (12.5–15) keV, it increases to 0.53. Analysis of the *S*-parameter curve of the nonannealed sample 510 (Figure 25b) allows to conclude that positron-sensitive defects are almost absent throughout the whole coating depth. This means that annihilation occurred mainly with the electrons of the defect-free areas. Therefore, the value of the *S*-parameter was minimal and equal to 0.49. As a result of annealing at 873 K, the value of the *S*-parameter increased significantly to 0.53 in the surface layer of the coating. The value of the *S*-parameter further increased at the positron energy of 14–17 keV and approached the maximum possible value 0.59. It should be mentioned that the *S*-parameter depends on both the concentration and the type of vacancy defects, at which positrons are captured and subsequently annihilate there in the areas of low electron density [54–56].

AQ12

Since a grain size of the nanostructured coatings is smaller than a length of positron diffusion track in

defect-free nanograin, all positrons can reach the grain surface and consequently the interfaces. In this case, most of the volume of available information concerns the defects in the interfaces and triple or more joints. Since the grain size in our experiments varies from 40 to 60 nm, the volume fraction of the interfaces may reach 30–35 vol.%, and the interfaces of triple joints may be about 5–10 vol.%, and then almost all positrons have to be captured along the interfaces [54].

According to results presented in Ref. [58], the total fraction of interfaces can be evaluated as

$$V_{Si} = 1 - \frac{\left[3S \cdot (L/S)\right]}{L^3} \approx \frac{3S}{L} \tag{1}$$

where

L is the grain size

S is the interface width (the near-interface zone)

A fraction of the inherent grain interfaces is

$$V_{Ii} = \frac{3S \cdot (L/S)}{L^3} \tag{2}$$

And a fraction of triple joints is

$$V_{Ti} = V_{Si} - V_{Ii} \tag{3}$$

If the distance between the defects is essentially shorter than the positron diffusion length, all positrons have to be captured by defects; that is, we observe the capture saturation. In this case, the positron lifetime spectrum contains only one component [54,55], and the S-parameter of Doppler broadening seems to have a maximum value.

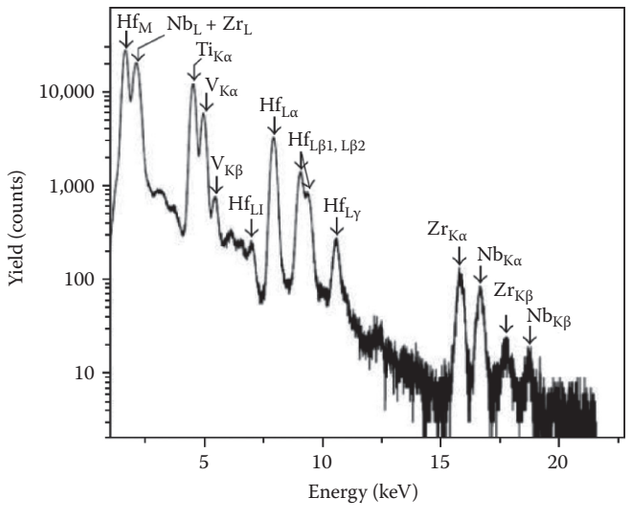

FIGURE 26 A common PIXE spectrum (in a logarithmic scale) obtained from sample 512, when it was irradiated by a proton beam of 1.4 MeV energy.

Figure 26 shows the integral spectrum obtained by PIXE of the element concentrations for (Ti–Zr–Hf–V–Nb)N coatings number 512 after annealing at 873 K (30 min). We can evidently see the redistribution of elements over the depth after thermal annealing. Studying these spectra, we found all the elements constituting the nanostructured coating. As it will be shown later in the text, the μ-PIXE element distribution maps taken from the (Ti–Zr–Hf–V–Nb)N coating before and after annealing up to 873 K in Figure 29a and b can be seen.

The x-ray diffraction data for sample 512 show formation of a strong texture with the (111) axis, which is perpendicular to the plane of growth (Figure 27). The data of x-ray strain measurements indicate that sample 512 is characterized by

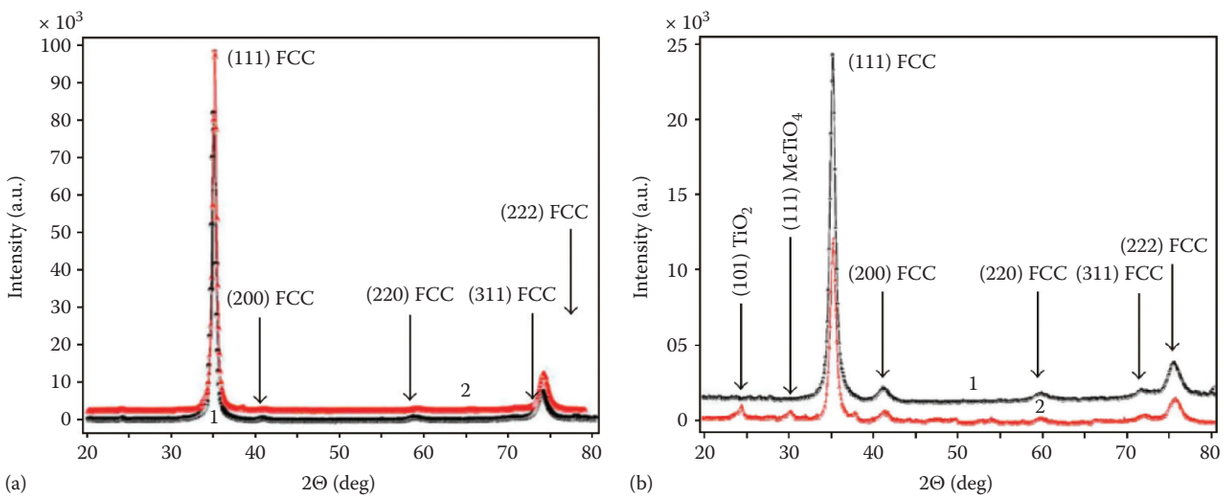

FIGURE 27 (a) The XRD spectra for a coating fabricated at $P_N = 0.7$ Pa and $U_b = -200$ V (sample 512): (1) before annealing and (2) after thermal annealing. (b) The XRD spectra of a coating fabricated at $P_N = 0.2$ Pa and $U_b = -50$ V (sample 510): (1) before annealing and (2) after thermal annealing at 873 K.

the highest value of a lattice period in a stress-free cross section (α = 0.442 nm). It correlates with the results of the elemental analysis, according to which the highest concentration of nitrogen is observed when the working pressures of coating deposition are high. An appearance of biaxial texture with (111) and (110) axes at U_{bias} = −200 V resulted in the formation of coatings with the highest hardness reaching 58–60 GPa and very uniform and smooth surfaces [10,56–58]. In this case, thermal annealing does not significantly change a structure–phase state of the coatings (Figure 27a). However, it reduces a little the deformed state of compression from the strain ratio of 2.76% in the initial state (as-deposited state) to 2.59% after annealing.

It was found that there was only a slight increase from 56 to 68 nm of crystal size and a decrease from 0.4424 to 0.4386 Å of lattice constant, with an increase of annealing temperature from R_T to 873 K. The barely changed structure and grain size during high-temperature annealing are believed to be attributed to the small driving force because of the low grain boundary energy and low kinetics from the sluggish diffusion. The grain boundary energy comes from the energy difference between the state of grain boundaries and that inside the grains. The large lattice distortion effect because of large atomic size difference (the atomic size of Ti, 1.462 Å; V, 1.316A Å; Zr, 1.603 Å; Hf, 1.578 Å; Nb, 3.301 Å; Zr, 1.603 Å; Hf, 1.578 Å) can markedly raise the overall free energy of crystalline structure.

Therefore, the actual grain boundary energy was largely lowered, leading to a very small driving force for coarsening. A detailed mechanism has been proposed by Huang and Yeh [60] in case of (AlCrNbSiTiV)N coating. The sluggish diffusion originating from the higher packing density because of the packing of atoms with different sizes made the effective diffusion distances very short, which led to the enhanced difficulty of grain growth. Regarding the lattice decline, the following three possible factors must be considered: composition variation, phase separation, and residual stress.

At lower pressures of deposition P_N = 0.1, the decrease of the lattice period in stress-free sections was observed at 0.438 nm, which seemed to be associated with a lower content of nitrogen atoms in the coating. Annealing of sample 510 not only led to a significant change of the stress–strain state but also of the phase composition (see Figure 27b, curve 2). These figures show that sample 510 demonstrates a decrease of the intensity of textured reflexes of an FCC metallic crystal lattice (compare spectra 1 and 2 in Figure 27b). In this case, nitrogen atoms are in the form of the FCC sublattice shifted by 1/2 space diagonal forming the so-called NaCl structural lattice type. The appearance of reflections at small angles was also observed, corresponding to the formation of oxides of TiO_2 (JCPDS 01-0562) and oxide-type $MeTiO_4$, where Me corresponds to the content of Zr and Hf. The structural type of this oxide is similar to an oxide of an isostructural (allomeric) $ZrTiO_4$ (JCPDS 07-0290) and $HfTiO_4$ (JCPDS 14-0103). Upon annealing of the sample, the strain state of compression decreased from −1.9% (before annealing) to −0.7% (after annealing).

A characteristic form of α-$\sin^2\psi$ plots for high-entropy metallic coating with a bcc lattice and a nitride one with an FCC metallic lattice of NaCl type is demonstrated in Figure 28. We can see that a compressing deformation exceeding 2% was developing in the CAVD coatings. Inclination angles of the plots are different for all investigated nitride coatings and crystalline groups of definite textures in this work (Figure 28, plots 2 and 3). According to Roy's model of stress uniformity [15,52], such difference indicates an essential contribution of oriented microstresses of the deformation mode, surveyed by the α-$\sin^2\psi$ method. In this case, if a region of the uniform microdeformation is comparable to the crystallite size, the latter demonstrates anisotropy of an elastic modulus. In the

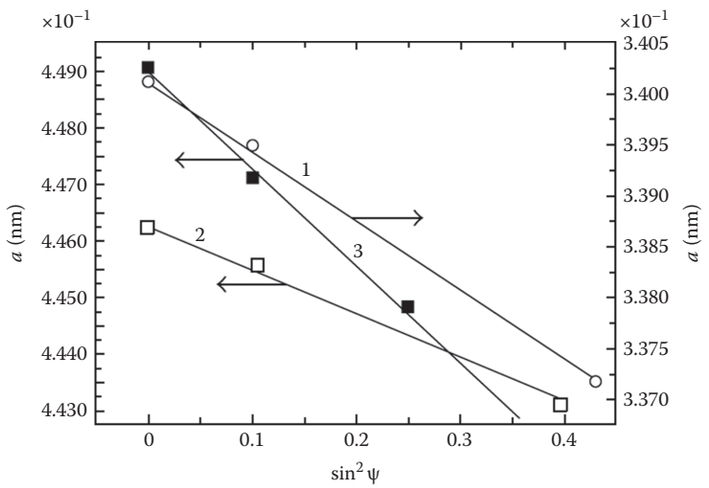

FIGURE 28 Dependences of α-$\sin^2\psi$ obtained for the texture axis (110) of a high-entropy alloy Ti–V–Zr–Nb–Hf deposited in a nitrogen-free atmosphere (1), for the texture axis (111) (a straight line 2) and (110) (a straight line 3),which was the coating of the highest hardness (58–60 GPa) deposited in the nitrogen atmosphere at P_N = 0.27 Pa and U_b = −200 V, using a method of crystalline groups.

case of complexes of textured crystallites, such deformation can be considered as a factor of nonuniformity of stresses and deformations due to intercrystalline interactions [10,22]. Measurements of the material elastic characteristics, which were performed using the macro- and microbeams and calculated according to Vegard's rule, along with the element analysis indicated that a period of crystalline lattice were about 0.3371 nm for the high-entropy coating $Ti_{0.23}$–$V_{0.05}$–$Zr_{0.07}$–$Hf_{0.078}$–$N_{0.49}$. This value corresponds to that of the stress-free cross section $2\nu/(1 + \nu) = 0.45$ in terms of those plotted for this α-$\sin^2\psi$ coating (plot 1, Figure 28), where ν is the Poisson coefficient. From here $\nu = 0.29$, and the elastic strain of compression developing in such coating has the value of 2.2 GPa. The previously mentioned approach can be applied for calculations of stresses in the nitride single-axis oriented coatings. In the case of double-axis orientation (plots 2 and 3, Figure 28), application of averaged meaning allows us only to perform a correct evaluation of the deformed state of the crystal lattice.

The results of RBS (Figure 2a and b) and EDX analyses for the samples 510 (for which the value of the 512) indicated that two peaks are formed on the curve of *S*-parameter when the energy of the positron beam is (3 ÷ 5) keV and (14 ÷ 17) keV. This can be explained by the increased diffusion process of both nitrogen and oxygen atoms near the surfaces of sample 510. This indicates the appearance of new channels for the annihilation of positrons, which are more efficiently attracted by defects, which appeared at the interface as a result of annealing and formed the new quasi-amorphous and nanostructured phases of nitrides. This conclusion is supported by the results of μ-PIXE analysis, which indicated that an oxide film was formed on the surface, and therefore the value of *S*-parameter increased. In the coating depth, the elements are redistributed, which confirmed the assumption about the end of the process of spinodal segregation and the formation of new phases along nanograin interfaces [10,15,22,57,58]. It must be noted that the grain growth during annealing is the most obvious mechanism of structural relaxation. The segregation of nitrogen at the grain interfaces hampers the growth of nanocrystals.

Evaluation of the nanograin size by XRD, according to the Debye–Scherrer equation, gave the nanograin size of 55 ÷ 58 nm for sample 512, which did not change after thermal annealing. Evaluation of the diffusion length of positrons was $L + \approx 100$ nm, which was essentially longer than the size of nanograins. According to the conventional interpretation, the nanopores are primarily placed at the lines of intersection of three or more interfaces. Thus, the ratio of intensities of the positron lifetime components should decrease with the increase of crystallite size. It was confirmed by theoretical and experimental studies [15,54–56]. Therefore, reduction of the *S*-parameter (sample 512) may be connected to the annealing of interface vacancies, resulting in a decrease of the *S*-parameter intensity [14,62,63].

Moreover, additional nanopores may appear due to the vacancy agglomeration taking place in the process of crystallite growing, even if the latter is not very significant. This may result in the increase of the *S*-parameter. This was reported in the work of [58], where the intensity of the second component of positron lifetime increased.

As it follows from the RBS (Figure 24a and b) and EDX analyses, the strongly structured coatings (sample 512) with a high level of compressive strain in the as-deposited states (–2.76%) demonstrate the high oxidation resistance after annealing. This occurred due to low oxygen diffusion to the coating depth and a high degree of filling of the octahedral interstitials by nitrogen atoms during the deposition of coating under conditions of high nitrogen pressure in the chamber. Thus, this system does not form a nitride interlayer between nanograins, due to the low diffusion resulting from high compressive stresses. It seems that the annealing temperature is insufficient or the energy of atoms is too low to form the interlayer. Therefore, the main channel allowing the nitrogen atoms to sink for the formation of the nitride interlayer is the interphase *coating–substrate* boundary (see the *S*-parameter curve of the maximum value 0.53 at 13–14 keV energy of analyzing positron beam).

Figure 29a shows the 3D map of the element distribution in the area of 2.5 × 2.5 μm for sample 512, with scanning step 0.5 μm. As we can see in this figure, the elements are distributed almost evenly over the surface and in the bulk. At the same time, thermal annealing up to 873 K (for 30 min, at 100 Pa pressure in chamber) leads to the segregation of impurities at the grain interfaces, and the maps of these distributions clearly indicate these regions (see Figure 29b). We pay attention to the fact that almost all the elements forming the coating are arranged, and since the PIXE method is insensitive to nitrogen, the spectrum does not indicate it. The width of these interfaces is about 0.12 ± 0.25 μm, and the size of large grains reaches up to 0.3–0.8 μm. Thus, considering the results of XRD analysis and μ-PIXE with *S*-parameter before and after annealing, we can say that in the structure of (Ti–Zr–Hf–V–Nb)N, the grains of 0.3–0.8 μm with nanograins of 45–60 nm fragmented into them are formed. Dimensions of these nanograins were determined by XRD. After annealing, the impurities are segregated at the interfaces of large grains due to thermostimulated diffusion, and an interphase interlayer is formed at small grains as an agglutinating phase.

The results of research obtained by electron diffraction microscope (TEM) demonstrated that the structure–phase state of coatings with different contents of alloying elements (Si, B, Al) in the TiN system even at high diffusion mobility of atoms (i.e., at deposition temperature 673–773 K) formed the two-phase textured grain structures. The grains with a submicron size of 0.2–0.6 μm in such systems were fragmented by the low-angle interfaces with the disorientation angles of 5° and by nanograins of 20–30 nm [20].

According to Refs. [12,20,42], increasing the content of low solubility alloying elements, upon reaching their critical concentration and/or diffusion mobility, leads to enrichment of interfaces of growing crystals with these elements (taking into account the values of mixing entropy of separate nitrides,

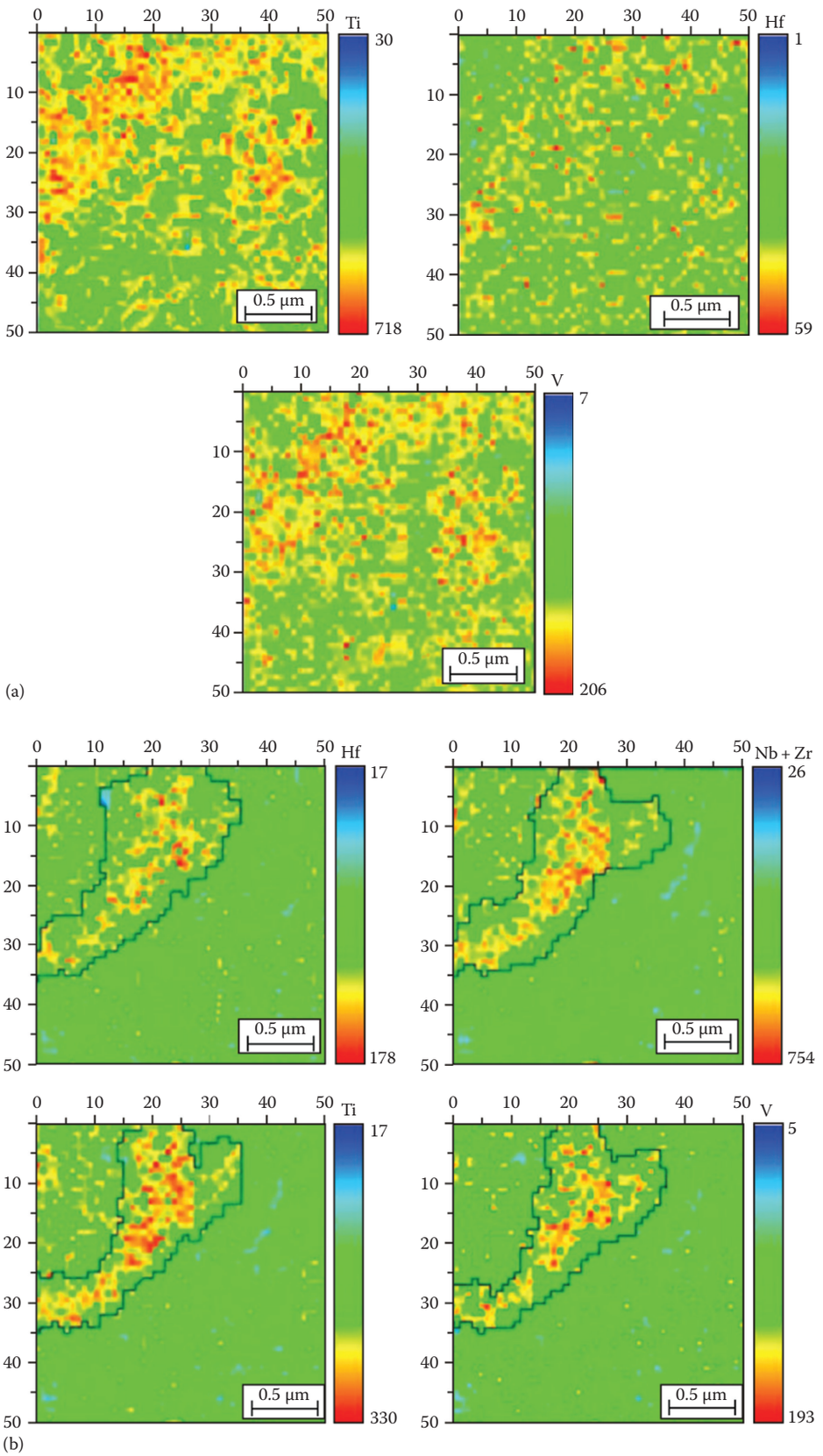

FIGURE 29 Maps of the element distribution in the area of 2.5 × 2.5 μm (the raster of 50 × 50, the step size of 0.5 μm) for sample 512 before (a) and after (b) annealing.

TABLE 10
Enthalpies of Formation (ΔH) of the Five Binary Nitrides

	TiN	VN	ZrN	HfN	NbN
ΔH, kJ/mol	−337.7	−217.2	365.3	−373	−234.7

presented in Table 10, and also the total entropy of all metals and nitrides on its basis included to the coatings) and to the corresponding decrease of the grain size [64]. This effect, along with the nonequilibrium deposition conditions, promoted the formation of randomly oriented nanocrystallites. It should be noted that the maximum nanohardness of H = 58 GPa was obtained also for sample 512. Elastic modulus for these samples reached the value of E = 618 GPa. For samples 509 and 510, hardness values were of little lower rates, – 52 GPa and 46 GPa, respectively.

Analysis of the wear by-products, wear track structure (on the sample), and wear spots (on counterface ball) was provided along with the microscopic study of the wear track structure on the coating surface and the change of wear spots on the ball. Measurement of the vertical section of wear tracks was performed by profilometry in four diametrically and orthogonally opposite fields and determined the average cross-sectional area and wear tracks. Figure 30 presents the results of the tribological wear test of the steel substrate. The vacuum-arc coatings of Ti–Zr–Hf–Nb–V (4.0 mm thick) were deposited in the nitrogen reaction gas environment on the polished steel disk. The results of the friction tests showed the increase of the surface roughness due to the drop component of the plasma flow (see Figure 31 and Table 11).

Deposition of coatings on the substrate of steel 45 provides an increased durability, thus reducing the wear of steel. The study of friction tracks is of great interest, which can give information about the mechanism of wear. Figure 32 shows photographs of friction tracks in vacuum-arc coating (Ti–HF–Nb–Zr–V)N. Results of the study of wear products in the friction process for the coating (Ti–HF–Nb–Zr–V)N–Al_2O_3 counterface are shown in Figure 33.

Finally, we can say that this chapter reports original results revealing the mechanisms of formation of interfaces in multicomponent coatings and formation of the stress states of nanocrystals, as well as their effect on thermal diffusion of nitrogen and oxygen atoms. We found that by changing the deposition conditions, it is possible to influence the thermal stability and hardness of multicomponent nanostructured coatings. We also considered an effect of defect migration, which occurs in the process of annealing, on hampering the nanocrystal growth, when the annealing temperature increased. It turned out that the high-entropy nitride alloys and nanostructured coatings on their base contained only the single-phase solid solutions. Its structure was composed of the submicron grains of 0.3–0.8 μm, at the interfaces of which the interlayers of impurity atoms were formed. At the same time, the fragmented nanograin structures of 40–60 nm size with subgrains of the nitride phases were formed in the submicron grains. The sluggish diffusion originating from the higher packing density because of the packing of atoms with different sizes made the effective diffusion distances very short, which led to the enhanced difficulty of grain growth. Regarding the lattice decline, the following three possible factors must be considered: composition variation, phase separation, and residual stress.

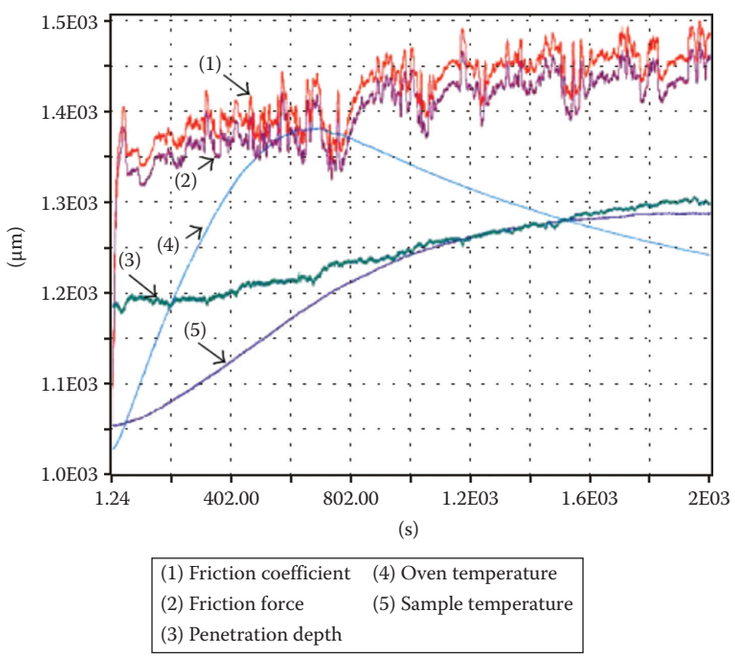

FIGURE 30 Results of tribological tests of the steel substrate (steel 45).

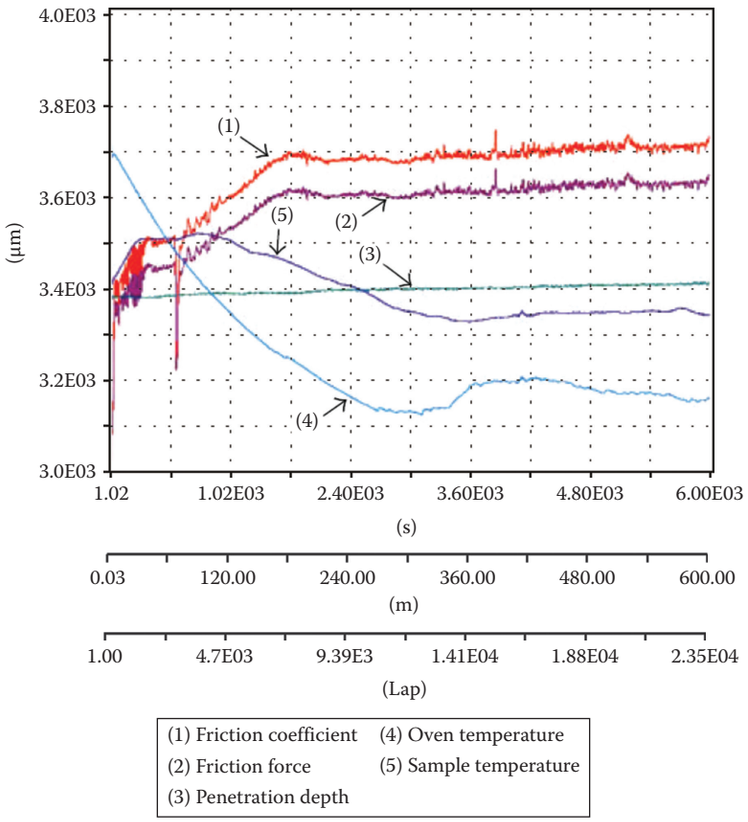

FIGURE 31 The results of tribological tests of the "steel 45 + coating (Ti–HF–Nb–Zr–V)N–Al_2O_3 counterface."

TABLE 11
Tribological Characteristics of the Different Systems Based on Ti, Zr, Hf, Nb, V, and N

	Friction Coefficient, μ		Wear Factor, $mm^3 \times H^{-1} \times nm^{-1}$	
Sample	**Initial**	**During Experiment**	**Of Counterface ($\times 10^{-5}$)**	**Of Sample ($\times 10^{-5}$)**
Coatings Ti–Hf–Nb–Zr–V–N	0.221	1.030	1.12	0.027
Steel 45	0.204	0.674	0.269	35.36

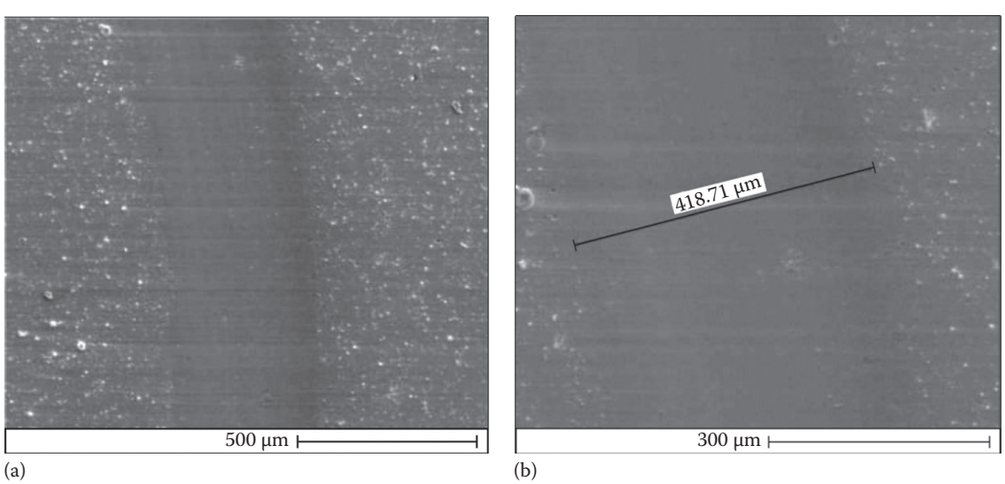

FIGURE 32 Photographs of the surface morphology of friction: (a) general view and (b) friction track.

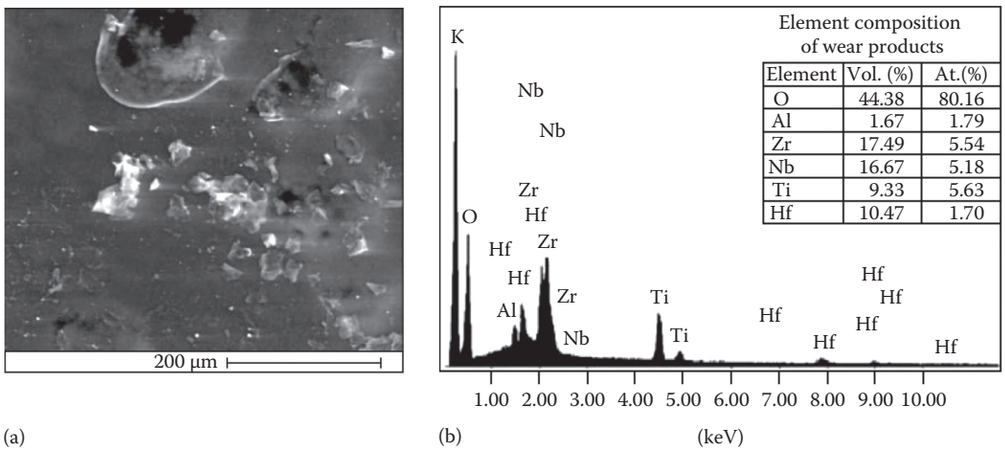

FIGURE 33 Micrograph of (a) wear products and (b) its energy spectrum.

CONCLUSION

Main results concerning fabrication and researching of superhard nanostructure coatings based on (Ti–Hf–N)Fe, Ti–Hf–Si–N, and (Ti–Hf–Zr–V–Nb)N are presented in the work. Such coatings were fabricated using the cathodic-PVD method under different deposition conditions, such as substrate bias potential, residual pressure, deposition velocity, and nitrogen or Ar/N mix feeding velocity. The main mechanisms of fabrication of nanocomposites with small nanograins from solid solutions, surrounded by 1 or 2 α-SiN_x amorphous phase monolayers, were studied. It is shown in the chapter that significant micro- and macrostresses appear in the coatings, which allows us to manipulate nitrogen and oxygen diffusion. In observable coatings we found high 56 GPa hardness (so-called superhardness), good resistance to oxidation under high temperatures (up to 1300°C), and high tribotechnical properties. Using unique methods of analysis (slow positron beam, proton microbeam μ-PIXE, XRD, α-sinψ^2 method, SEM with microanalysis, RBS, and SIMS), we studied diffusion, mass transfer, and segregation processes on the nanograin border interfaces. We detected the special influence of segregated impurities and vacancy-type defects on the electron structure, hardness, and other properties of nanocomposite coatings.

ACKNOWLEDGMENTS

The work was done under the aegis of two budget programs N 0112U001382 and N 0113U000137 of the Ukrainian Ministry of Education and Science.

REFERENCES

1. Pogrebnjak A.D., Bondar O.V., Sobol O.V., Beresnev V.M. Changing of defect's structure and properties of superhard nanostructured Ti-Si-N coatings, fabricated using CPVD, before and after annealing. *Soft Nanoscience Letters* 3 (2013): 46–51.
2. Pogrebnjak A.D. Investigation of element profiles, defects, phase composition and physical and mechanical properties of superhard coatings Ti-Hf-Si-N. *Materials Sciences and Applications* 4 (2013): 24–31.
3. Pogrebnjak A.D., Beresnev V.M. Hard nanocomposite coatings, their structures and properties. In Ebrahimi, F. ed., *Nanotechnology and Nanomaterials, Nanocomposites-New Trends and Developments*, Rijeka, Croatia: InTech, 2013.
4. Pogrebnjak A.D. Structure and properties of nanostructured (Ti-Hf-Zr-V-Nb)N coatings. *Journal of Nanomaterials* (2013), 12 pp.
5. Gleiter H. Nanocrystalline materials. *Progress in Materials Science* 33 (1989): 233–315.
6. Siegel R.W. Cluster-assembled nanophase materials, *Annual Review of Materials Science* 21 (1991) 559–579.
7. Veprek S., Reiprich S.A. Concept for the design of novel superhard coatings. *Thin Solid Films* 268 (1995) 64–71.
8. Pogrebnjak A.D., Shpak A.P., Azarenkov N.A., Beresnev V.M. Structures and properties of hard and superhard nanocomposite coatings. *Physics-Uspekhi* 52 (2009): 29–54.
9. Mayrhofer P.H., Mitterer C., Hultman L., Clemens H. Microstructural design of hard coatings. *Progress in Materials Science* 51 (2006): 1032–1114.
10. Musil J. Hard and superhard nanocomposite coatings. *Surface and Coatings Technology* 125 (2000) 322–330.
11. Andrievski R.A. Nanomaterials based on high-melting carbides, nitrides and borides. *Russian Chemistry Reviews* 74 (2005): 1061–1072.
12. Musil J. Hard nanocomposite coatings: Thermal stability, oxidation resistance and toughness. *Surface and Coatings Technology* 207 (2012): 50–65.
13. Pogrebnjak A.D., Ponomarev A.G., Shpak A.P., Kunitskii Yu.A. Application of micro- and nanoprobes to the analysis of small-sized 3D materials, nanosystems, and nanoobjects. *Physics-Uspekhi* 55 (2012): 270–300.
14. Pogrebnjak A.D., Ruzimov Sh.M., Alontseva D.L. et al. Structure and properties of coating on Ni-base deposited using plasma jet before and after electron beam irradiation. *Vacuum* 81(10) (2007): 1243–1251.
15. Krause-Rehberg R., Leipner H.S. *Positron Annihilation in Semiconductors: Defect Studies*. Berlin, Germany: Springer-Verlag, 1999.
16. Pogrebnjak A.D., Il'yashenko M.V., Kaverin M.V. et al. Physical and mechanical properties of the nanocomposite and combined Ti-N-Si/WC-Co-Cr/and Ti-N-Si/$(Cr_3C_2)_{75}$-$(NiCr)_{25}$ coatings. *Journal of Nano- and Electronic Physics* 1 (2009): 66–77.

17. Pogrebnyak A.D., Mahmud A.M., Karasha I.T., Kirik G.V., Tkachenko R.Y., Sypylenko A.P. Structure and physical-mechanical properties of nc-TiN coatings obtained by vacuum-arc deposition and deposition of HF discharge. *Journal of Nano- and Electronic Physics* 3 (2011): 97–105.
18. Pogrebnjak A.D., Beresnev V.M., Demjanenko A.A. et al. Adhesive strength, superhardness and the phase and elemental composition of nanostructured coatings based on Ti-Hf-Si-N. *Physics of the Solid State (Rus)* 54(9) (2012): 1882–1890.
19. Pogrebnjak A.D., Beresnev V.M., Kaverina A.Sh. et al. Formation of superhard Ti-Hf-Si-N/Nb-N/Al_2O_3 multilayer coatings for highly effective protection of steel. *Technical Physics Letters* 39(2) (2013): 189–192.
20. Pogrebnjak A.D., Beresnev V.M., Kolesnikov D.A. et al. The effect of segregation and thermodiffusion on the formation of interfaces in nanostructured (Ti-Hf-Zr-V-Nb)N multielement coatings. *Technical Physics Letters* 39(3) (2013): 280–283.
21. Pogrebnjak A.D., Sobol O.V., Beresnev V.M. et al. Phase composition, thermal stability, physical and mechanical properties of super- hard on base Zr-Ti-Si-N nanocomposite coatings. *Nanostructured Materials and Nanotechnology IV: Ceramic Engineering and Science Proceedings* 31(7) (2010): 127–138.
22. Pogrebnyak A.D., Ponomarev A.G., Kolesnikov D.A. et al. Effect of mass transfer and segregation on the formation of superhard nanostructured Ti-Hf-N(Fe) Coatings. *Technical Physics Letters* 38(7) (2012): 623–626.
23. Gale W.F., Totemeier T.C. *Smithells Metals Reference Book*. Oxford, U.K.: Butterworth Heinemann, 1976.
24. Grafutin V.I., Ilyukhina O.V., Myasishcheva G.G. et al. Positronics and nanotechnologies: Possibilities of studying nanoobjects in materials and nanomaterials by the method of positron-annihilation spectroscopy. *Physics of Atomic Nuclei* 72(10) (2009): 1672–1681.
25. Kansy J. Programs for positron lifetime analysis adjusted to the PC windows environment. *Materials Science Forum* 652 (2001): 363–365.
26. Grafutin V.I., Prokop'ev E.P. Positron annihilation spectroscopy in materials structure studies. *Physics Uspekhi* 45(1) (2002): 59–74.
27. Konarski P., Iwanejko I., Mierzejewska A., Diduszko R. Morphology of working environment microparticles. *Vacuum* 63(4) (2001): 679–683.
28. Konarski P., Iwanejko I., Mierzejewska A. SIMS depth profiling of working environment nanoparticles. *Applied Surface Science* 203–204 (2003): 757–761.
29. Pogrebnyak A.D., Shpak A.P., Beresnev V.M. et al. Stoichiometry, phase composition, and properties of superhard nanostructured Ti-Hf-Si-N coatings obtained by deposition from high frequency vacuum-arc discharge. *Technical Physics Letters (Russian)* 37(7) (2011): 636–640.
30. Khomenko A.V., Lyashenko I.A. A stochastic model of stick-slip boundary friction with account for the deformation effect of the shear modulus of the lubricant. *Journal of Friction and Wear* 31(4) (2010): 308–316.
31. Misaelides P., Hadzidimitrion A., Noli F., Pavlidou E., Pogrebnjak A.D. Investigation of the characteristics and corrosion resistance of Al_2O_3/TiN coatings. *Applied Surface Science* 252(23) (2006): 8043–8049.
32. Pogrebnyak A.D., Sobol' O.V., Beresnev V.M. et al. Features of the structural state and mechanical properties of ZrN and Zr(Ti)-Si-N coatings obtained by ion-plasma deposition technique. *Technical Physics Letters* 35(10) (2009): 925–928.
33. Pogrebnjak A.D., Ruzimov Sh.M., Alontseva D.L. et al. Structure and properties of coatings on Ni base deposited using a plasma jet before and after electron a beam irradiation. *Vacuum* 81(10) (2007): 1243–1251.
34. Gleiter H. Tuning the electronic structure of solids by means of nanometer-sized microstructures. *Scripta Materialia* 44 (2001): 1161–1168.
35. Musil J. Physical and mechanical properties of hard nanocomposite films prepared by reactive magnetron sputtering. In Cavaleiro A., De Hosson J.Th.M., eds., *Nanostructured Coatings*, pp. 407–463. New York: Springer Science+Business Media, LCC, 2006.
36. Pogrebjank A.D., Shpak A.P., Azarenkov N.A., Beresnev V.M. Structure and properties of hard and superhard nanocomposite coatings. *Physics-Uspekhi* 52(1) (2009): 29–54.
37. Musil J., Šatava V., Zeman P., Čerstvý R. Protective Zr-containing SiO_2 coatings resistant to thermal cycling in air up to 1400°C. *Surface and Coatings Technology* 203 (2009): 1502–1507.
38. Musil J., Hromádka M., Novák P. Effect of nitrogen on tribological properties of amorphous carbon films alloyed with titanium. *Surface and Coatings Technology* 2005(2) (2011): S84–S88.
39. Pogrebnyak A.D., Bratushka S.N., Malikov L.V. et al. Effect of high doses of N+, N+ + Ni+, and Mo++ W+ ions on the physicomechanical properties of TiNi. *Technical Physics* 54(5) (2009): 667–673.
40. Pogrebnyak A.D., Shpak A.P., Beresnev V.M. et al. Stoichiometry, phase composition, and properties of superhard nanostructured Ti-Hf-Si-N coatings obtained by deposition from high-frequency vacuum-arc discharge. *Technical Physics Letters* 37(7) (2011): 636–639.
41. Beresnev V.M., Sobol' O.V., Pogrebnjak A.D., Turbin P.V., Litovchenko S.V. Thermal stability of the phase composition, structure, and stressed state of ion-plasma condensates in the Zr-Ti-Si-N system. *Technical Physics* 55(6) (2010): 871–873.
42. Korotaev A.D., Borisov D.P., Moshkov V.Y., Ovchinnikov S.V., Pinzhin Y.P. Tyumentsev A.N. Elastic stress state in superhard multielement coatings. *Physical Mesomechanics* 12(5–6) (2009): 269–279.
43. Blinkov I.V., Volkhonsky A.O., Anikin V.N., Petrzhik M.I., Derevtsova D.E. Phase composition and properties of wear-resistant Ti-Al-Cr-Zr-Nb-N PVD coatings. *Physics and Chemistry of Materials Processing (Russian)* 4 (2010): 37–43.
44. Lin S.-Y., Chang S.-Y., Huang Y.-C., Shieu F.-S., Yeh J.-W. Mechanical performance and nanoindenting deformation of (AlCrTaTiZr)NC_y multi-component coatings co-sputtered with bias. *Surface and Coatings Technology* 206(24) (2012): 5096–5102.
45. Pogrebnjak A.D., Beresnev V.M. *Nanocoatings, Nanosystems, Nanotechnologies.* Sharjah, UAE: Bentham Science, 2012.
46. Pogrebnjak A.D., Shpak A. P., Beresnev V.M. et al. Effect of thermal annealing in vacuum and in air on nanograin sizes in hard and superhard coatings Zr-Ti-Si-N. *Journal of Nanoscience and Nanotechnology* 12 (2012): 9213–9219.
47. Chang H.-W., Huang P.-K., Yeh J.-W., Davison A., Tsau C.-H., Yang C.-C. Influence of substrate bias, deposition temperature and post-deposition annealing on the structure and properties of multi-principal-component (AlCrMoSiTi)N coatings. *Surface and Coatings Technology* 202(14) (2008): 3360–3366.
48. Lai C.-H., Cheng K.-H., Lin S.-J., Yeh J.-W. Mechanical and tribological properties of multi-element (AlCrTaTiZr)N coatings. *Surface and Coatings Technology* 202(15) (2008): 3732–3738.

49. Lai C.-H., Tsai M.-H., Lin S.-J., Yeh J.-W. Influence of substrate temperature on structure and mechanical, properties of multi-element (AlCrTaTiZr)N coatings. *Surface and Coatings Technology* 201(16–17) (2007): 6993–6998.
50. Yeh J.-W., Chen Y.-L., Lin S.-J., Chen S.-K. High-entropy alloys – A new era of exploitation. *Materials Science Forum* 560 (2007): 1–9.
AQ23 51. http://www.simnra.com.
52. Azarenkov N.A., Sobol' O.V., Pogrebnjak A.D., Beresnev V.M. *Engineering Vacuum-Plasma Coatings*. Kharkov, Ukraine: Academy of Kyungpook National University, 2011.
53. Shaefer H.E. Investigation of thermal equilibrium vacancies in metals by positron annihilation. *Physica Status Solidi* 102(1) (1987): 47–65.
54. Rempel' S.V., Gusev A.I. Surface segregation in decomposing carbide solid solutions. *JETP Letters* 88(7) (2008): 435–440.
55. Wurschum R., Farber P., Dittmar R., Scharwaechter P., Frank W., Schaefer H.-E. Thermal vacancy formation and self-diffusion in intermetallic Fe_3Si nanocrystallites of nanocomposite alloys. *Physical Review Letters* 79(24) (1997): 4918–4921.
56. Lavrent'yev V.I., Pogrebnjak A.D., Sandrik R. Evolution of vacancy defects in the surface layers of a metal irradiated with a pulsed electron beam. *JETP Letters* 65(8) (1997): 651–655.
57. Veprek S. The search for novel, superhard materials. *Journal of Vacuum Science & Technology A* 17(5) (1999): 2401–2421.
58. Gusev A.I. *Nanomaterials, Nanostructures and Nanotechnology*. Moscow, Russia: Fizmatlit, 2005.
59. Chang S.-Y., Lin S.-Y., Huang Y.-C., Wu C.-L. Mechanical properties, deformation behaviors and interface adhesion of $(AlCrTaTiZr)N_x$ multi-component coatings. *Surface and Coatings Technology* 204(20) (2010): 3307–3314.
60. Huang P.-K., Yeh J.-W. Effects of nitrogen content on structure and mechanical properties of multi-element (AlCrNbSiTiV)N coating. *Surface and Coatings Technology* 203(13) (2009): 1891–1896.
61. Tsai D.-C., Huang Y.-L., Lin S.-R., Liang S.-C., Shieu F.-S. Effect of nitrogen flow ratios on the structure and mechanical properties of (TiVCrZrY)N coatings prepared by reactive magnetron sputtering. *Applied Surface Science* 257(4) (2010): 1361–1367.
62. Pogrebnjak A.D., Sobol' O.V., Beresnev V.M. et al. Phase composition, thermal stability, physical and mechanical properties of superhard on base Zr-Ti-Si-N nanocomposite coatings. *Ceramic Engineering and Science Proceedings* 31(7) (2010): 127–138.
63. Pogrebnjak A.D., Bakharev O.G., Pogrebnjak N.A. Jr. et al. Certain features of high-dose and intensive implantation of Al ions in iron. *Physics Letters A* 265(3) (2000): 225–232.
64. Misaelides P., Hatzidimitriou A., Noli F., Pavlidou E., Pogrebnjak A.D. Investigation of the characteristics and corrosion resistance of AlO/TiN coatings. *Applied Surface Science* 252(23) (2006): 8043–8049.

AUTHOR QUERIES

[AQ1] Please provide expansion of the acronym "HF" if appropriate.
[AQ2] The acronym "RBS" has been used for the following expansions: "Rutherford backscattering" and "Rutherford ion backscattering". Please check.
[AQ3] RBS has been defined as "Rutherford backscattering" in text and "Rutherford ion backscattering" in Figure caption 17. Please check.
[AQ4] Please spell out the abbreviations XPS, EDX, XRD, CAVD at the first instance, if appropriate.
[AQ5] Please provide expansion of the acronyms "XPS and μ-PIXE" if appropriate.
[AQ6] Figure 5 will be printed in grayscale. Please rephrase mention of color.
[AQ7] Both "N" and "n" have been used in the subscript of "P." Please check the usage for correctness.
[AQ8] Please check sentence starting "In case of…" for clarity.
[AQ9] Please check whether "(7)" should be changed to "(1)" in Figure caption 10.
[AQ10] Please provide part label caption (c) in Figure caption 13.
[AQ11] Please check sentence starting "Investigated, that a…" for clarity.
[AQ12] Please check the figure citation inserted in the sentence "Analysis of S-parameter curve ... " for correctness.
[AQ13] The "S" in "S-parameter" appears both in italics and roman throughout the text. Please check and make one form consistent.
[AQ14] Please provide expansion of the acronym "bcc" if appropriate.
[AQ15] Please check sentence starting "In the case…" for clarity.
[AQ16] Please check sentence starting "The results of…" for clarity.
[AQ17] Please confirm whether the citation of Figure 2a nd b could be changed to Figure 3a and b.
[AQ18] The expansion and abbreviation for "TEM" do not seem to match. Please check.
[AQ19] Please provide expansion of the acronym "PVD" if appropriate.
[AQ20] Original references 33, 62, 40, 64 seem to be repetitions of references 14, 21, 29, 31, respectively. Also references 43, 44, 47–51 are not cited in the text and the existing reference citations are not in sequential order. Please provide missing in-text citations for references deleting the repetitions and maintaining sequential order of citations.
[AQ21] Please provide page range for ref. 3.
[AQ22] Please provide volume number for Ref. [4].
[AQ23] Please provide author group, article title, year, and accessed date for ref. 51.